energy&fuels

pubs.acs.org/EF
Article

A Silicon Oxide–Carbon Anode with High Reversibility for Na-Ion Batteries

Edoardo Barcaro, Daniel Amato, Stiven Forti, Camilla Coletti, and Jusef Hassoun*

Cite This: *Energy Fuels* 2026, 40, 3408–3422
Read Online

ABSTRACT: Amorphous carbon (AC) represents nowadays the most widespread anode for sodium-ion batteries (SIBs). Herein, we blended silicon oxide and few-layer graphene (FLG) within an AC matrix achieved by hydrothermal treatment and annealing of sucrose to get a highly reversible anode for SIBs. The composite has partially amorphous character with graphitic reflections, various functional groups, and micrometric morphology including submicron-to-nano particles. The anode reveals reversible electrochemical activity within various potential regions vs Na^+/Na, accounting for Na-insertion/deposition with partial alloying with Si between 0.01 and 0.1 V, the Na-intercalation between 0.1 and 0.50 V, and Na-solvent complex cointercalation at a potential higher than 0.60 V. Galvanostatic cycling in sodium half-cells shows for the material a maximum capacity of ∼180 mAh g^{-1}, with retention between 93 and 94% over 400 cycles, and average Coulombic efficiency exceeding 99%. The Na-ion full-cell exploiting the anode in a diglyme-based electrolyte and a sodium-deficient layered cathode operates at ∼3 V, with an initial capacity of 100 mAh g^{-1} retained over 300 cycles for 63%, and a mean Coulombic efficiency value of 99.97%. These findings suggest the composite anode and the Na-ion battery setups exploited in this work are promising for sustainable energy storage applications, tracking the way of Li-ion batteries.

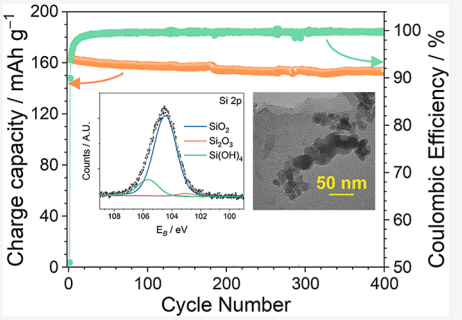

1. INTRODUCTION

Among the raising tools for energy storage, SIBs are considered one of the most promising to guarantee a sustainable power supply for next-generation devices.[1] This battery can in principle operate similarly to the Li-ion battery (LIB), according to the alkali-ion rocking-chair pathway, without concerns ascribed to the spotted distribution of lithium, raising prices, and limited material viability.[2] Indeed, sodium is abundant, has a moderate price, and has adequate energy content, which is boosted by its low redox potential of −2.71 V vs standard hydrogen electrode (SHE).[3] Several works focused on layered metal oxides for SIB cathodes, involving Ni\Co\Mn in various ratios[4,5] and including Al/Mg/Ti within the cathode formulation to enhance the electrochemical response.[6−9] Therefore, an 18650-type cylindrical SIB based on the layer-oxide cathode and hard-carbon anode has been recently commercialized.[10] Besides this class of cathode materials, polyanionic compounds, Prussian blue, and its analogues have also been intensively studied to identify the most suitable trade-off for SIB diffusion.[4] Regarding the anode side, the focus has been principally devoted to hard carbons (i.e., non-graphitized ones)[11,12] and metal-oxide compounds.[13] Hard carbon appeared of actual interest since it can be derived from numerous natural products or even wastes by adopting adequate carbonization processes but is unfortunately affected by low volumetric capacity.[12,14−17] On the other hand, hard/amorphous carbons have gained significant attention as sustainable substrates for energy storage due to their advantageous features including disordered character, controllable porosity, and rich surface functionality, whose interplay dictates the anode electrochemical performance.[18] These materials foresee various alkali-ion storage mechanisms such as adsorption, intercalation, and pore-filling, which overall can influence their reversible capacity and cycling stability.[12,19−21] Meanwhile, graphite, i.e., the most widespread and successful anode in the LIB industry, with a specific capacity of 372 mAh g^{-1}, mainly evolving below 0.2 V vs Li^+/Li, has been only marginally exploited for SIB due to its quite low capacity, modest compatibility with carbonate-based Na-aprotic electrolytes, and limited stability of binary graphite cointercalation compounds.[22−25] In principle, graphitic character can facilitate the kinetics of the cointercalation process since the desolvation energy may be very low or absent. Indeed, the ability to cointercalate the solvent within the structure to form a stable ternary compound was unraveled around a decade ago, exploiting sodium salts in glyme-based electrolyte media.[26,27] Therefore, the employment of graphitic materials should be tuned considering their massive use in LIB systems due to Li-

Received: December 9, 2025
Revised: January 12, 2026
Accepted: January 14, 2026
Published: January 29, 2026

intercalation ability, as well as in several other fields due to high electrical and thermal conductivity.[28] In this scenario, further anode materials operating at low voltage versus Na^+/Na with adequate Na-storage ability and specific capacity appeared to us to welcome enhanced energy density in full-cell configuration, and to avoid at the same time dendrite formation. Among them, silicon oxide−carbon anodes have been selected due to the wide interest arising from their successful application in LIBs.[29−36]

1.1. Content and Aim of This Research

We report in this work the synthesis and characterization of a composite anode formed by FLG and SiO_2 embedded in AC for application in SIBs. The FLG is a commercial substrate of stacked tents of graphene layers that confers to the material a partially graphitic character,[37] while the AC matrix is derived by annealing a sucrose precursor dissolved in a water/alcohol dispersion of FLG and SiO_2. The latter precursor is expected to stabilize the structure and possibly contribute, after a partial reduction at 800 °C under Ar/H_2, to the anode capacity by Na alloying. The synthesis, previously developed by exploiting different C to SiO_2 ratios for application either in LIBs or in Li-ion sulfur batteries,[38,39] is performed through an environmentally compatible hydrothermal process. In this work, the anode is characterized in terms of structure, chemical properties, morphology, and performance in Na half- and full-cells. The impact of the highly reversible anode has been characterized by using both Cu and a less expensive/heavy Al current collector, which can be advantageously employed in Na cells.[40] The data evidenced that both FLG and AC contribute well to the material capacity in the Na cell, while SiO_2, which is usually considered an insulator, has a non-negligible electrochemical activity when included within the carbonaceous framework. On the other hand, this outcome matched the results already achieved in our previous studies exploiting analogue materials in the LIB environment.[38,39] Accordingly, the composite anode has revealed reversible Na^+ storage within its structure through multiple-step electrochemical processes involving both the crystalline/amorphous-carbon and SiO_2 components. Considering the suitable electrochemical performance, the anode has been tested in a laboratory-scale SIB using a layered oxide cathode and a glyme-based electrolyte and exploiting the favorable replacement of the Cu current collector with Al, which is expected to enhance the energy density of the system. The Na-ion cell, operating at about 3 V with high reversibility and relevant Coulombic efficiency (99.97% mean value upon 300 cycles), has been considered a suitable energy storage system for complementary applications to LIBs, such as small consumer electronics.

2. EXPERIMENTAL SECTION

2.1. Synthesis of the Composite Anode

The SiO_2/FLG/AC anode material, hereafter indicated as SiO_xC, was prepared by slightly modifying a synthesis previously proposed for LIBs.[38,39] Accordingly, 2.40 g of sucrose (≥99.0%, Fluka Analytical) was dissolved in 20 mL of a solution composed of distilled water and isopropanol (1:1 volume ratio) and added to a mixture of 0.25 g of amorphous silicon dioxide powder (SiO_2, silica, average particle size 0.007 μm, Sigma-Aldrich) and 0.25 g of FLG (produced by BeDimensional S.p.A.).[37] The mixture was sonicated at 50 °C for 2 h and transferred into an autoclave reactor, which was heated at 190 °C for 12 h and then cooled to room temperature. This process yielded a brownish-hue compound, which was retrieved from the autoclave and dried on a plate at 70 °C until complete solvent evaporation. Thereafter, the compound is exposed to an Ar/H_2 flow (5% H_2, Air Liquide Italia) inside a tubular furnace, preconditioned at 100 °C (1 h time frame, temperature increase rate of 5 °C min^{-1}), then annealed at 800 °C (6 h time frame, temperature increase rate of 10 °C min^{-1}), and finally cooled down to room temperature. The obtained material was ground into an agate mortar to obtain a fine black powder, later employed as an electrochemically active material to satisfy the sodium ion housing within the electrode. AC used as a blank was prepared by drying a sucrose solution at 100 °C and annealing using the same condition adopted above for the SiO_xC composite.

2.2. Synthesis of the $Na_{0.48}Al_{0.03}Co_{0.18}Ni_{0.18}Mn_{0.47}O_2$ Cathode

The P2/P3-type layered sodium cathode, $Na_{0.48}Al_{0.03}Co_{0.18}Ni_{0.18}Mn_{0.47}O_2$ (indicated with the acronym NCAM), was synthesized through a coprecipitation route following an optimized method reported in previous works.[8,9] Aluminum nitrate nonahydrate ($Al(NO_3)_3{\cdot}9H_2O$, Sigma-Aldrich, ≥98%), cobalt(II)-nitrate hexahydrate ($Co(NO_3)_2{\cdot}6H_2O$, Sigma-Aldrich, ≥99.0%), nickel(II)-nitrate hexahydrate ($Ni(NO_3)_2{\cdot}6H_2O$, Sigma-Aldrich, ≥98.5%), and manganese(II)-nitrate tetrahydrate ($Mn(NO_3)_2{\cdot}4H_2O$, Sigma-Aldrich, ≥97.0%) were dissolved in deionized water to form a solution observing the 1:2:2:4.5 molar ratio with respect to Al/Co/Ni/Mn. A 0.5 M NaOH aqueous solution was dropwise added to the nitrate solution to precipitate a hydroxide precursor (50 mol % excess with respect to the hydroxide). The hydroxide precursor was filtered, washed various times with deionized H_2O, and dried as below: overnight at 70 °C and then for 12 h at 120 °C in a dry air flow. Next, the precursor was mixed with sodium hydroxide (NaOH pellets, Sigma-Aldrich, ≥98%) in the 1:1 molar ratio. The resulting precursor was calcined at 500 °C for 5 h in a dry air flow, then ground in a mortar, pelletized, calcined at 1000 °C for 6 h in a dry air flow, naturally cooled, rinsed with excess of deionized water, filtered, dried under a vacuum at 100 °C, and then stored in a dry ambient.

2.3. Material Characterization

The structure of the SiO_xC powder was investigated by X-ray diffraction (XRD) through a Bruker D8 Advance instrument equipped with a Cu Kα radiation source scanning the 10°−60° 2θ range using a step size of 0.02° and a rate of 10 s $step^{-1}$. The composition of the material was studied by thermogravimetric analysis (TGA) performed within the 25 − 1000 °C temperature range using a heating rate of 5 °C min^{-1} in dry air flow with a Mettler-Toledo TGA 2 instrument (Mettler-Toledo, Columbus, OH, USA). Fourier-transform infrared (FT-IR) spectra were recorded via a Bruker Vertex V70 instrument set up in transmittance mode in a wavenumber range from 400 to 4000 cm^{-1}. The SiO_xC powder morphology was investigated by scanning electron microscopy (SEM) through a Zeiss Gemini SEM 460 relying on a zirconium oxide-coated-tungsten field emission gun, exploiting the secondary electron mode and using an in-lens objective lens, while transmission electron microscopy (TEM) and selected area electron diffraction (SAED) patterns were carried out by means of a Talos L120C-G2 (ThermoFisher) equipped with a LaB_6 thermionic electron gun operating at 120 kV. X-ray photoelectron spectroscopy (XPS) measurements were carried out using a Specs XR50 source with an Al anode at a power of 300 W. The analyzer employed was a Specs Astraios 190 with a 2D-CMOS detector and a 3 × 25 mm entrance slit. All the high-resolution spectra were acquired with a pass energy of 10 eV in normal emission conditions. All spectra were fitted first by iteratively calculating a Shirley background and then using a linear combination of Voigt single peaks (or doublets) for all related signals, except for the C 1s sp^2 signal, for which a Gaussian-broadened Doniach−Sunjic line shape has been used. The components are explicitly shown in the plots and described in the legends, together with the resulting envelope function.

2.4. Electrode Casting and Characterization

The electrode tapes were prepared by casting via a doctor blade tool (MTI Corp.) of slurries formed by 80 wt % active material powder, which was either SiO_xC or NCAM,[8,9] a 10 wt % polyvinylidene

https://doi.org/10.1021/acs.energyfuels.5c06312
Energy Fuels 2026, 40, 3408−3422

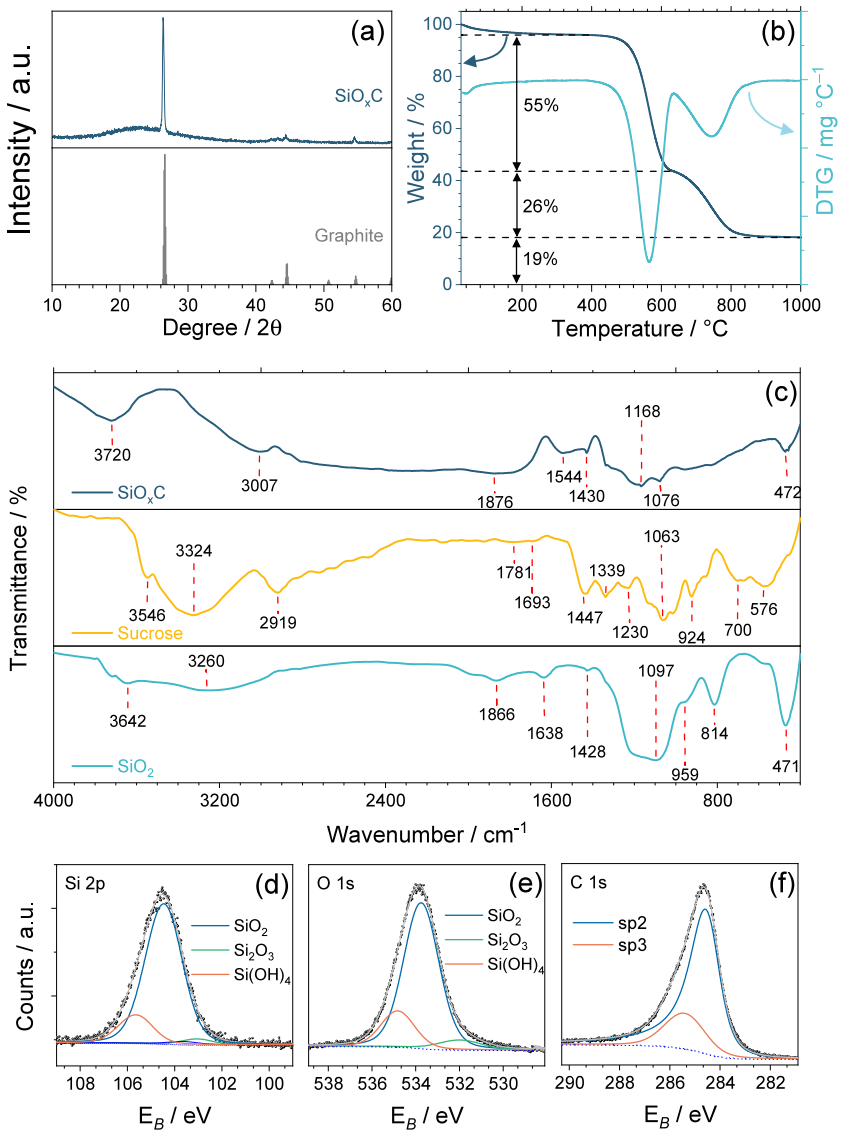

Figure 1. Physical−chemical characterization of the SiO_xC powder, in detail: (a) X-ray diffractograms for the SiO_xC sample; reference data for graphite (ICSD #76767) is reported for comparison; (b) TGA performed under dry air flow with a heating rate of 5 °C min^{-1} from 25 to 1000 °C and corresponding DTG; (c) FT-IR spectra acquired in transmittance mode of SiO_xC powder, sucrose, and SiO_2 from 4000 to 400 cm^{-1} wavenumbers; (d−f) XPS core-level spectra of (d) Si 2p, (e) O 1s, and (f) C 1s of the SiO_xC powder.

fluoride (PVdF 6020, Solef) polymer binder, and a 10 wt % carbon black (super P carbon, Timcal, indicated as CSP) electron conductor, dispersed in *N*-methyl-2-pyrrolidone (NMP, Sigma-Aldrich). The slurries were cast onto Al (thickness of 20 μm, MTI Corp.) for NCAM and either onto Cu (thickness of 10 μm, MTI Corp.) or Al for SiO_xC, and dried at 70 °C inside an oven equipped with a peristaltic pump to remove the NMP solvent. The obtained foils were calendared using an MSK-2150 Rolling Machine (MTI Corp.) to achieve a thickness of 70% with respect to the original tapes, usually within the range of 120−130 μm. The tapes were cut into discs with diameters of 10 and 14 mm (0.785 and 1.54 cm^2 geometric areas, respectively) using dedicated Nogami hand-held punches. The electrodes were dried under vacuum for 2 h at 110 °C inside a Büchi oven and finally stored inside an Ar-filled glovebox (MBraun, O_2 and H_2O contents lower than 1 ppm). The active material loading of the electrodes was 2.0−6.2 mg cm^{-2} for SiO_xC and 2.3−5.9 mg cm^{-2} for NCAM (always clarified in the figure caption whenever an electrode is tested). The above procedure was also adopted for casting on Cu the material constituents, i.e., either SiO_2, FLG, or AC, dispersed in NMP solvent with CSP and PVdF (80:10:10 weight ratio, respectively), to achieve blank electrodes for the sake of comparison with SiO_xC. The SiO_xC electrode morphology was investigated by SEM through a Zeiss Gemini SEM 460 relying on a zirconium oxide-coated-tungsten field emission gun, exploiting the secondary electron mode. The structure of the electrode was investigated by XRD through a Bruker D8 Advance instrument equipped with a Cu Kα radiation source scanning the 10°−60° 2θ range using a step size of 0.02° and a rate of 10 s $step^{-1}$. Either pristine or cycled electrodes tested in the Na cell using the glyme electrolyte over 100 cycles at 0.05 A g^{-1} within the 0.01−2.0 V range were investigated.

2.5. Electrolytes

The electrolytes used in this work are (i) tetraethylene glycol dimethyl ether (TEGDME, $CH_3(OCH_2CH_2)_4OCH_3$, Sigma-Aldrich) dissolving sodium triflate ($NaCF_3SO_3$, 98%, Sigma-Aldrich) salt with a concentration of 1 mol_{salt} $kg_{solvent}^{-1}$ (1 m), indicated in the text with the acronym TE-F, and (ii) diethylene glycol dimethyl ether (DEGDME, $CH_3(OCH_2CH_2)_2OCH_3$, Sigma-Aldrich) dissolving sodium hexafluorophosphate ($NaPF_6$, 99.9% trace metals basis, anhydrous, battery grade, Merck) salt with a concentration of 1 mol_{salt} $L_{solution}^{-1}$ (1 M), indicated in the text with the acronym DE-P.

https://doi.org/10.1021/acs.energyfuels.5c06312
Energy Fuels 2026, 40, 3408−3422

Before employment, TEGDME and DEGDME were stored under molecular sieves (rods, 3 Å, size 1/16 in., Honeywell Fluka, dried under a vacuum at 270 °C for 3 days, cooled down, and stored under Ar) until a H_2O content lower than 10 ppm was achieved as determined by a Karl Fischer 899 Coulometer (Metrohm). $NaCF_3SO_3$ salt was dried for 2 days under a vacuum at 110 °C to remove water traces and stored under Ar.

2.6. Electrochemical Characterization

CR2032 coin-type cells (MTI Corp.) and 3-electrode T-type Swagelok cells (10 mm diameter electrodes) were assembled inside an Ar-filled glovebox (MBraun, O_2 and H_2O contents lower than 1 ppm) by stacking, respectively, a 14 or 10 mm diameter sodium metal disc (99.9%, Sigma-Aldrich, trace metal basis) cut from sodium pieces, roll pressed, and finally punched as counter and reference electrodes; a 16 or 10 mm diameter glass fiber (Whatman GF/B) disc as a separator soaked with the electrolyte (amount fixed, respectively, to 50 and 200 μL for coin cells and T-cells); and either a SiO_xC or NCAM disc as a working electrode. The adopted cell setup is indicated in each figure caption. The electrochemical features of SiO_xC and its constituents (i.e., SiO_2, FLG, and AC) were examined through cyclic voltammetry (CV) and electrochemical impedance spectroscopy (EIS), employing a VersaSTAT MC Princeton Applied Research (PAR-AMETEK) multichannel potentiostat at room temperature. CV was performed in 3-electrode T-type cells within the 0.01−2.0 V vs Na^+/Na potential range at a scan rate of 0.1 mV s^{-1}, while EIS spectra were collected at the open circuit voltage (OCV) condition before cycling and upon 1, 5, and 10 CV runs using an alternate voltage signal of 10 mV in the frequency range between 500 kHz and 100 mHz. The EIS spectra were fitted using the nonlinear least-squares (NLLS) method within the Boukamp notation by accepting only fits with a χ^2 value of the order of 10^{-4} or lower.[41,42] The fitting enabled us to describe the Nyquist spectra in terms of equivalent circuits, including resistive (R) and constant phase elements (CPE, Q), in detail: (i) R_e is the electrolyte resistance, indicated by the high-frequency intercept of the plot; (ii) (R_iQ_i) is associated with the high-medium frequency semicircle accounting for the electrode/electrolyte interphase; and (iii) Q_w is ascribed to the semi-infinite Warburg-type Li^+ diffusion, depicted by a low-frequency tilted line.

2.6.1. Half-Cell Galvanostatic Cycling. The Na|TE-F|SiO_xC coin cells were galvanostatically cycled between 0.01 and 2.0 V either at a constant current rate of 0.05 A g^{-1} or by applying various current rates increasing every 10 cycles from 0.015 A g^{-1} to 0.03, 0.06, 0.09, and 0.15 A g^{-1} before decreasing back to 0.015 A g^{-1} after the 50th cycle. Subsequently, the latter current was held for 60 discharge/charge runs, and the cells were subject again to the above-reported current rate variations. To investigate the contributions in the sodium cell of the SiO_xC constituents, Na|TE-F|SiO_2, Na|TE-F|FLG, and Na|TE-F|AC coin cells were galvanostatically cycled between 0.01 and 2.0 V using a constant current rate of 0.05 A g^{-1}. The Na|DE-P|SiO_xC coin cell was galvanostatically cycled between 0.01 and 2.0 V by applying various current rates increasing every 10 cycles from 0.05 A g^{-1} to 0.1, 0.2, 0.3, 0.6, and 1.2 A g^{-1} (double current rate capability test) and decreasing back to 0.05 A g^{-1} after the 120th cycle. The galvanostatic cycling tests were performed via MACCOR series 4000 battery test systems (room temperature 25 °C, maximum fluctuation ±1.0 °C). Prior to galvanostatic tests, the cells were rested for 2 h. Naturally, the active material content within the electrode is accounted for by considering all the SiO_xC.

2.6.2. Na-Ion Full-Cell Exploiting the NCAM Cathode. The developed Na-ion full-cell configuration has been obtained by stacking the NCAM cathode just after casting and drying as indicated above and a chemically sodiated Na-SiO_xC anode. This chemical approach can advantageously compensate for the initial irreversible capacity of the anode and the sodium deficiency of the cathode by storing an adequate Na^+ amount to ensure efficient full-cell operation, as reported in our recent work.[43] Accordingly, the SiO_xC electrode (14 mm diameter, 1.54 cm^2 geometric area) was placed in direct contact with a Na foil wetted by DE-P and pressed with 0.2 kg weight. The partially sodiated Na-SiO_xC electrode was recovered upon 3 min of capillary contact, which was determined as a sufficient time frame to store a Na^+ amount for ensuring a proper cell balance. Subsequently, the Na-SiO_xC|DE-P|NCAM full-cell was galvanostatically cycled at the constant current rate of 0.05 A g^{-1} between 1.0 and 4.0 V. The current rate and capacity of the full-cell were referred to the cathode active material weight, while the cell balance and N/P capacity ratio were indicated along with the cell description in the Results and Discussion section.

3. RESULTS AND DISCUSSION

3.1. SiO_xC Physical−Chemical Characterization

Figure 1 reports some physical−chemical characteristics of the SiO_xC powder. The structure of the anode material is checked by means of XRD, as depicted by the pattern in Figure 1a, which shows a major narrow peak centered at 2θ = 26.4° corresponding to the graphite (002) plane reflection due to the partial stacking of the FLG sheets. The same diffractogram reveals a broad signal from 2θ = 13° to 2θ = 39°, which may be attributed to noncrystalline nanometric fumed silica used for the synthesis and the AC originating from the sucrose source, as indicated by a previous report for analogue materials used in LIB.[39] On the other hand, the latter work suggested that changing the ratio of the anode constituents does not influence the crystalline features of the final product; however, it could affect the sample's morphology and electrochemical response. Therefore, the weight ratio of silicon oxide and carbons within the composite anode is detected in Figure 1b through TGA, performed under air flow, and corresponding DTG. After the initial weight loss of 4% due to absorbed moisture within the material below 150 °C, the data evidence a substantial decay at 560 °C and a second one between 630 and 900 °C, ascribed to the removal of carbons in the anode as CO_2 gas formed by direct combustion with the oxygen in the air flow, leading to an overall C content of 81% and a residue of 19% corresponding to the SiO_x portion, both rescaled to exclude the water loss. Interestingly, if compared to a previous SiO_xC anode for LIBs,[39] the one reported herein shows a rather different composition, which is tuned for SIBs. Indeed, the magnitudes of the first loss associated with the more exposed amorphous carbon deriving from sucrose below 600 °C and the second one related to the more compact FLG occurring at higher temperature indicate for the two carbons a weight ratio of 55% and 26% in this SiO_xC, instead of 61% and 14% in the one developed for LIBs.[39] Furthermore, the silica residue above 800 °C is about 19%, rather than the 32% achieved in the previous work. The lower silica amount and higher FLG content compared to the material previously designed for a LIB can actually enhance the conductivity of the electrode to allow a more efficient operation in SIBs. Figure 1c shows the FT-IR spectra of the SiO_xC powder, including the synthesis sources (i.e., sucrose and SiO_2), while FLG is not taken into account due to its negligible contribution to the IR signal.[38] In fact, this material has an almost pure graphitic IR response since it is prepared by exfoliation of bulk graphite crystals using high-speed solvent jet streams, without significant formation or addition of any functional group.[37] As expected, sucrose reveals a wide signal at 3324 cm^{-1} due to the vibrational modes of O−H in the intermolecular hydrogen bond from hydroxyl substituents, as well as C−H vibrational signals at 2919 cm^{-1} due to $-CH_3/-CH_2$ aliphatic groups, 1781 cm^{-1} due to C═O stretching of −COO in acetyl esters, 1693 and 1447 cm^{-1}, respectively, due to asymmetric and symmetric modes of O−H

https://doi.org/10.1021/acs.energyfuels.5c06312
Energy Fuels 2026, 40, 3408−3422

Table 1. Signal Indexing of the FT-IR Spectra of SiO_xC, Sucrose, and SiO_2 Sources Reported in Figure 1c

	wavenumber [cm^{-1}]	assignments		group	ref
SiO_xC	3007	$\nu_{(C-H)}$	$-CH_3/-CH_2/-CH$	aliphatic/olefinic groups or aromatic rings	44
	1876	$\nu_{(C=O)}$	$-O-CO-O-$	organic carbonates	48
	1544	$\nu_{(C=C)}$	$-C=C-$	olefinic groups or aromatic rings	49
	1430	$\delta_{(H-C-H)}$	$-CH_2$	substituted aliphatic groups	45
	1168	$\nu_{(C-O)}$	C−OH and C−O−C	phenols and carboxylic acids or ethers	49
	1076	$\nu_{(Si-O)}$	Si−O−Si	siloxane groups	45
	472	$\nu_{(Si-O)}$	Si−O−Si	siloxane groups	45
Sucrose	3324	$\nu_{(O-H)}$	−OH	intermolecular hydrogen bond from hydroxyl substituents	44
	2919	$\nu_{(C-H)}$	$-CH_3/-CH_2$	aliphatic groups	44
	1781	$\nu_{(C=O)}$	−COO	acetyl ester	44
	1693	$\nu_{asimm(O-H)}$	−COO	carboxylic or carbonyl groups	44
	1447	$\nu_{simm(O-H)}$	−COO	carboxylic or carbonyl groups	44
	1063	$\nu_{(C-O)}$ or $\nu_{(C-C)}$	C−O−C or −C−C-	carboxylic or carbonyl groups	44
SiO_2	3260	$\nu_{(O-H)}$	−OH	hydroxyl on silanol groups	45
	1638	$\delta_{(H-O-H)}$	H_2O	adsorbed water	46
	1428	$\delta_{(O-CO-O)}$	Si−O−CO−O−Si	carbonates from CO_2 impurities	47
	1097	$\nu_{(Si-O)}$	Si−O−Si	siloxane groups	45
	959	$\nu_{(Si-OH)}$	−SiOH	silanol groups	45
	814	$\nu_{asimm(Si-O)}$	Si−O−Si	siloxane groups	45
	471	$\nu_{simm(Si-O)}$	Si−O−Si	siloxane groups	45

in carboxyl and carbonyl groups, and 1063 cm^{-1} ascribed to the C−O, C−C, C−O−C, or −C−C− stretching.[44] On the other hand, SiO_2 shows the signals of O−H hydroxyl stretching; however, due to silanol groups at 3260 cm^{-1},[45] a wave at 1638 cm^{-1} due to the H−O−H bending vibrations of adsorbed water,[46] and a signal at 1428 cm^{-1} ascribed to the O−CO−O bending in Si−O−CO−O−Si carbonates formed by CO_2 impurities.[47] Furthermore, the SiO_2 reveals the main signal at 1097 cm^{-1} ascribed to Si−O−Si asymmetric stretching in siloxane groups, a shoulder at 959 cm^{-1} due to the Si−OH stretching in silanol groups, a peak at 814 cm^{-1} for the symmetric stretching of Si−O−Si in siloxane groups, and a marked signal at 471 cm^{-1} for the bending of Si−O−Si in the same groups.[45] As for the SiO_xC, the spectrum appears quite different from the ones of the precursors, since the material is synthesized in reductive condition at 800 °C (see Experimental Section). Hence, the FT-IR evidence for the sample shows the typical signal at 3007 cm^{-1} ascribed to the C−H stretching modes in aliphatic/olefinic groups or aromatic rings,[44] and others at 1876 cm^{-1} due to stretching of C=O in organic carbonates.[48] In addition, a signal at 1544 cm^{-1} is due to stretching of C=C in olefinic groups or aromatic rings,[49] while the one at 1430 cm^{-1} is ascribed to H−C−H bending in substituted aliphatic groups.[45] Finally, further vibrations appear at 1168 cm^{-1} due to stretching of C−O, C−OH, and C−O−C in phenols and carboxylic acids or ethers,[49] at 1076 cm^{-1} due to stretching of Si−O−Si in siloxane groups, and at 472 cm^{-1} due to bending of Si−O−Si in siloxane groups.[45] For readers' convenience, Table 1 collects the signals achieved by the FT-IR spectra. In summary, the FT-IR study suggests that the SiO_xC sample is well functionalized with various groups, mainly originating from the formulation of the precursor and likely promoted by the synthetic process adopted herein. The presence of functional groups in the composite can likely promote the electrochemical performance of the anode; however, these groups could also increase the ratio of irreversible reactions, in particular during the initial stages of the cycling tests in the sodium battery, as indeed observed for analogue lithium cells.[38] The sample composition and the absence of contaminants are supported by the XPS analysis performed on the SiO_xC powder (see the survey spectrum in Figure S1 in the Supporting Information). Figure 1d displays the Si 2p core level spectrum, which is fitted with three components, the first of which (81%) is centered at 104.4 eV and reflects the signal from SiO_2 where the Si is in the +4 oxidation state.[50,51] Another component is centered at 105.5 eV (15%) and possibly attributed to $Si(OH)_4$, in which Si is still at a +4 oxidation state but with slightly higher binding energy.[52] The latter component well supports the FT-IR results, which suggest the presence of Si−OH silanol groups, possibly promoted by absorbed water for sample exposure to the atmosphere. The third component observed at 103.3 eV (4%) may be likely attributed to Si in the +2 oxidation state, e.g., a $SiO-SiO_2$ mixture, due to the partial reduction of the SiO_2 promoted by the H_2 at 800 °C during the synthesis (see Experimental Section for details). Furthermore, the signal recorded from O 1s in Figure 1e confirms the latter hypothesis by showing the same peak distribution (76%, 18%, and 6%) for the components at 533.8, 534.8, and 532 eV, respectively. On the other hand, the C 1s (Figure 1f) reveals a predominant component at 284.6 eV (78.5%), suggesting principally the sp^2 nature of the carbon, and a smaller component at 285.5 eV (21.5%) due to the sp^3 carbon contribution.

The morphology of the SiO_xC sample is investigated by SEM/TEM micrographs in Figure 2. The SEM image in Figure 2a shows micrometric agglomerates with a size of about 70 μm within a matrix including smaller dispersed particles. The magnified images in Figure 2b−d, as well as those reported in the Supporting Information (Figure S2), clearly reveal that both the agglomerates and the smaller particles are formed by an intimate mixture of FLG flakes, AC, and SiO_x. The TEM image of the FLG in Figure 2e and the inset of Figure S2g evidence the stacking of the graphene layers, with resulting polycrystallinity detected by SAED in the panel inset. On the other hand, the nanometric SiO_x spherules embedded in the AC matrix of the composite-anode powder are also detected in the TEM of Figure 2f and in the inset of Figure S2h. Therefore, we can describe the SiO_xC sample as an array in which carbons

https://doi.org/10.1021/acs.energyfuels.5c06312
Energy Fuels 2026, 40, 3408−3422

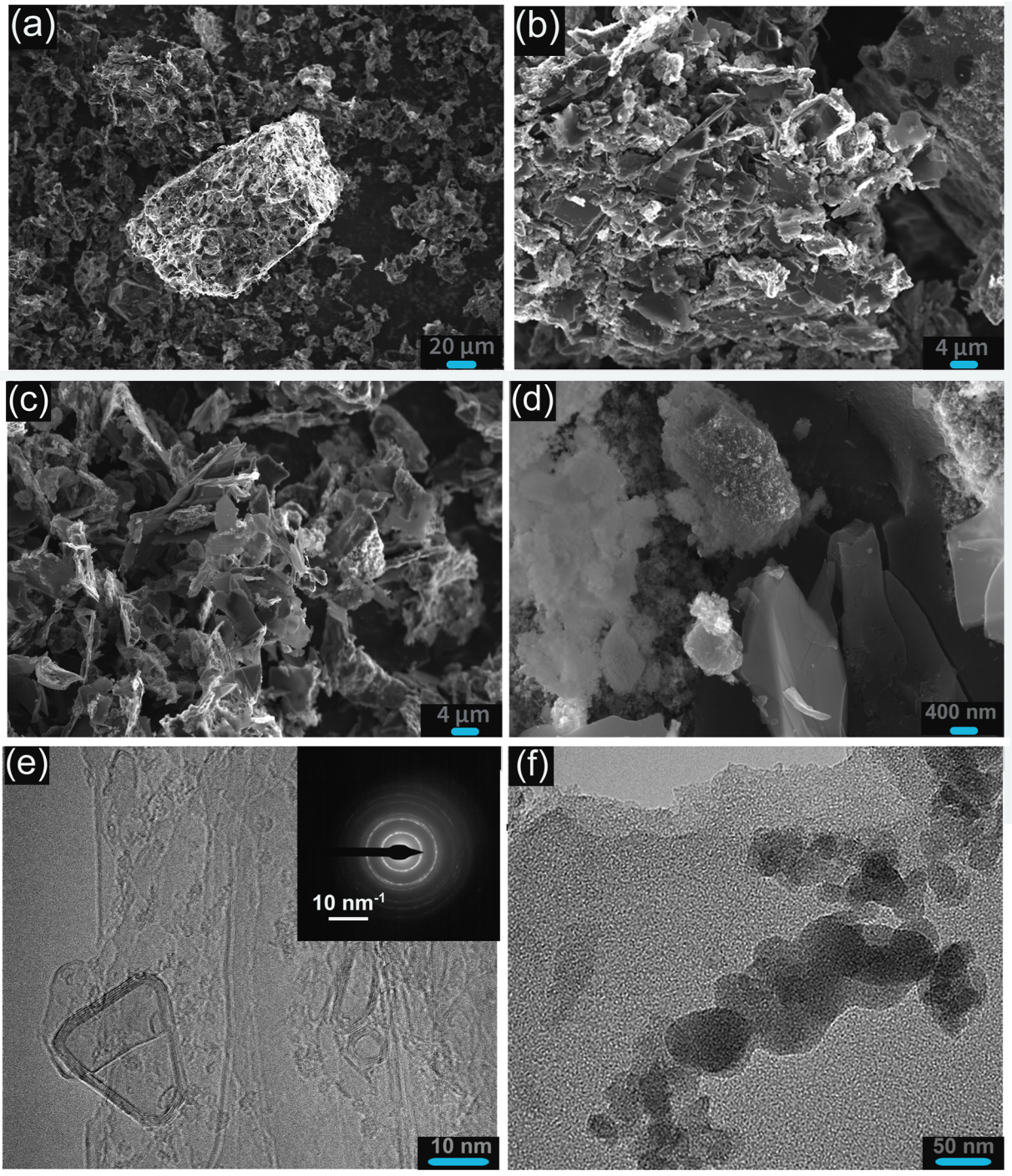

Figure 2. Morphological characteristics of the SiO_xC powder, in detail: (a–d) SEM images acquired in secondary electron mode using an in-lens objective lens. TEM images of (e) FLG pristine powder (inset reporting its SAED) and (f) SiO_xC powder.

of different natures (FLG, AC) and SiO_x are mixed to form a heterogeneous morphology, including an extended submicrometer matrix as well as 3D aggregates, despite the rigorous grinding process to which the sample is subjected. The composite submicrometric/micrometric shape of the sample may hold some advantages, such as enhanced electrochemical performance in SIB, structural stability, and high conductivity. Indeed, larger particles may limit the electrolyte decomposition and depletion upon cycling, which is instead triggered by the submicron particles. On the other hand, the small particles may improve the ion transport into the material by shortening the Na^+-diffusion paths.[53] Furthermore, as already suggested by the TGA results, SEM/TEM also indicates a different morphology of this sample compared to previous ones, due to the different ratio of the components (namely, SiO_2, FLG, and sucrose),[39] which may be more adequate to the Na-ion battery application.

3.2. Electrochemical Characterization of SiO_xC Electrodes

Figure 3 reports the investigation of the electrochemical features of the SiO_xC electrode cast onto either Al or Cu and studied in a sodium half-cell filled with the TE-F electrolyte, achieved by CV and EIS. The voltammograms reveal during

https://doi.org/10.1021/acs.energyfuels.5c06312
Energy Fuels 2026, 40, 3408–3422

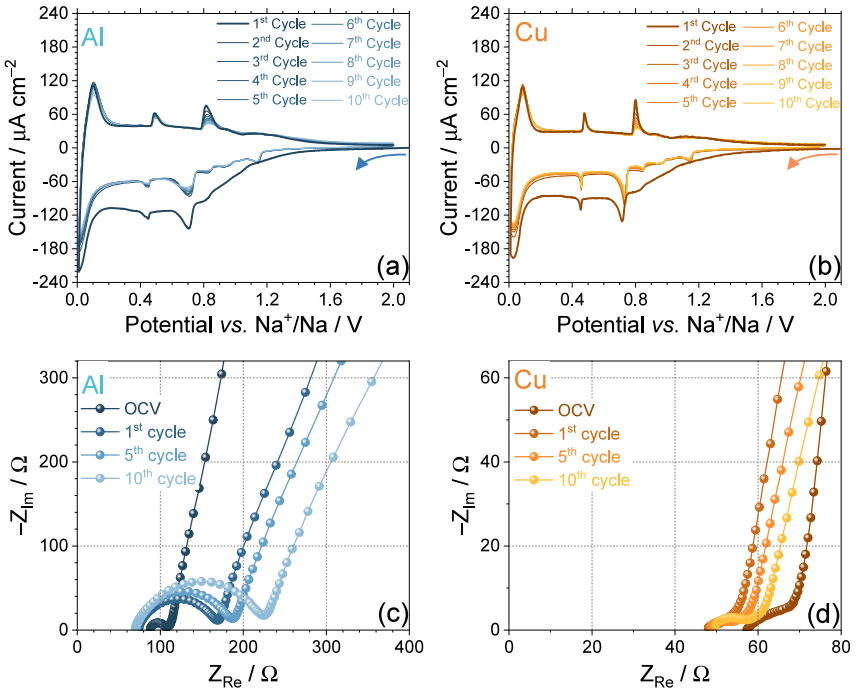

Figure 3. Electrochemical features of the SiO_xC electrode cast onto Al or Cu, in detail: (a,b) CV profiles and (c,d) Nyquist plots recorded by EIS related to Na|TE-F|SiO_xC T-cells; CV potential range: 0.01−2.0 V vs Na^+/Na; scan rate: 0.1 mV s^{-1}; EIS performed at the OCV cell condition and upon CV after the 1st, 5th, and 10th cycles between 500 kHz and 100 mHz; alternate voltage signal: 10 mV. Experiments were performed at 25 °C.

the first cathodic scan a broad wave with current onset beginning at about 1.30 V Na^+/Na, showing distinct peaks at 0.80, 0.70, 0.45, and 0.05 V vs Na^+/Na, which have comparable specific current and a narrowest shape using the Cu current collector (Figure 3b) rather than Al (Figure 3a). During the second cathodic scan, the CV peaks split to 6 resolved ones, while the broad wave between 1.30 and 0.00 V vs Na^+/Na vanishes, thus indicating partial irreversible reduction of the electrolyte with formation of the SEI at the electrode surface. This protective and conductive film is usually composed of NaF, Na_2CO_3, and/or other species within a thickness range of tenths of nm depending on the electrolyte composition and cycling experimental constraints.[54,55] The first anodic scan reveals 3 resolved peaks at 0.09, 0.49, and 0.80 V vs Na^+/Na, with a shoulder at 0.90 V vs Na^+/Na and a low-intensity wave between 0.9 and 1.30 V vs Na^+/Na, which are reproduced during the second run. The subsequent cycles show a remarkable overlapping of the above-mentioned anodic and cathodic peaks that appear to be the narrowest using Cu, with a slight current reduction and broadening of the oxidation process at about 0.80 V vs Na^+/Na and a similar trend for the reduction one at 0.70 V only for the sample using an Al current collector. The above slight shifts in the peak position and intensity may be ascribed to structural rearrangement of the electrode as well as to the consolidation and the stabilization of the SEI by the ongoing of the CV in the glyme-based electrolyte.[56] The various peaks described above in terms of position and intensity are hereafter assigned to specific Na^+ electrochemical processes exploiting additional CV tests carried out in Figure S3 (Supporting Information) on blank electrodes for SiO_xC, namely, FLG, AC, and SiO_2 cast onto Cu to maximize the signal. Indeed, the reversible peaks are coherent with the signals achieved from the blank samples, with a signature mainly ascribed to the cointercalation of solvated Na^+ into FLG at 0.70 V vs Na^+/Na and higher potentials, which is typical of the glyme-based electrolytes,[22] and the intercalation in the same carbon substrate of naked Na^+ at about 0.45 V vs Na^+/Na (compare Figures 3b and S3a). The sample also shows the insertion of Na^+ or deposition of Na principally into the AC at potentials near 0.00 vs Na^+/Na (compare Figures 3b and S3c). Instead, the contribution of the Na−Si alloying of SiO_2 appears very limited, with a modest signal at about 0.05 V vs Na^+/Na (Figure S3e). Therefore, we may summarize the CV response of the SiO_xC electrode in the Na cell as the combination of multiple processes, including the initial reductive decomposition with SEI formation (from 1.3 to 0.3 V vs Na^+/Na) and reversible processes accounting for Na^+-solvent cointercalation (from 1.3 to 0.7 V vs Na^+/Na), Na^+ intercalation (at about 0.45 V vs Na^+/Na), Na^+ insertion or deposition of Na principally into the AC near to 0.00 vs Na^+/Na, and limited Na−Si alloying at about 0.05 V vs Na^+/Na. The well-reversible response of the SiO_xC electrode can be justified by the stability of its interphase with the electrolyte, demonstrated by EIS spectra reported in Figure 3c,d recorded at the OCV condition of the half-cells and after 1, 5, and 10 CV scans. The NLLS analysis of the Nyquist plot allows the evaluation of resistive and constant phase elements (CPEs) of the cells through the description of each spectrum with an equivalent circuit. Accordingly, the cell can be represented by the $R_e(R_nQ_n)Q_w$ circuit, where (i) R_e is the electrolyte bulk resistance obtained as the high-frequency intercept of the plot with the x-axis; (ii) (R_nQ_n) elements (with n = 1, 2,···) account for the electrode/electrolyte interphase phenomena, such as charge transfer and SEI formation, identified by the high-middle frequency semicircles whose overall width leads to the total interphase resistance (R_i); and (iii) Q_w is a CPE due to the semi-infinite Warburg-type Na^+ ion diffusion represented by the tilted line at low-frequency values. The NLLS fitting results of the electrode cast on the Al and Cu current collectors, reported in Tables 2 and 3, reveal similar interphase

https://doi.org/10.1021/acs.energyfuels.5c06312
Energy Fuels 2026, 40, 3408−3422

Table 2. NLLS Analysis Carried Out on the Nyquist Plots Displayed in Figure 2c[a]

cell condition	circuit $R_e(R_iQ_i)Q_w$	R_1 [Ω]	χ^2
OCV	$R_e(R_1Q_1)Q_w$	23.7 ± 2.2	3×10^{-5}
after 1 CV	$R_e(R_1Q_1)Q_w$	95.9 ± 0.4	4×10^{-5}
after 5 CV	$R_e(R_1Q_1)Q_w$	116.3 ± 0.5	7×10^{-5}
after 10 CV	$R_e(R_1Q_1)Q_w$	155.4 ± 0.7	7×10^{-5}

[a]The impedance spectra were acquired on a Na|TE-F|SiO_xC cell, having the positive electrode cast onto Al, at the OCV and after 1, 5, and 10 CV runs, and fitted using the Boukamp software by exclusively accepting results with χ^2 values of the order of 10^{-5} or lower.

resistance at the OCV of 23.7 and 14.8 Ω, respectively. As soon as the first CV cycle is completed, the resistance values diverge; the one of the electrode using the Al current collector increases by almost 3 times (Table 2), while the one using the Cu shrinks by 1/3 (Table 3). The raising resistance of the electrodes cast on Al is most likely ascribed to possible corrosion of this current collector within reductive conditions and partial deterioration even by the action of the $CF_3SO_3^-$ anion.[57−59] Rather, the Cu current collector is much more stable, and the resistance of the electrode using it as the support decreases after the first CV, mostly due to a partial dissolution of the native SEI on SiO_xC. It is worth mentioning that the lower resistances of the material using Cu rather than Al also justify the narrowest shape of the CV peaks observed using the former current collector (also explained by its intrinsic higher-electron conductivity). On the other hand, the resistance increases with a relatively slower magnitude to about 155 Ω upon 10 cycles for the SiO_xC electrode on Al and to a value as low as 10 Ω during the same interval for the one on Cu as the SEI grows and finally stabilizes. The EIS trend of SiO_xC on Cu upon CV is almost identical to that of the blank electrodes cast on the same support, depicted in Figure S3b,d,f, with an interphase resistance ranging from 10 to 20 Ω (see Tables S1−S3 for NLSS analysis).

Therefore, we may state that the SiO_xC electrode can actually operate in SIBs with a multistep process characterized by modest polarization. Furthermore, the electrochemical process of the SiO_xC keeps its efficiency and low polarization; however, it has higher interphase resistance using an Al current collector rather than Cu, which has, instead, a relatively higher cost.[60]

3.3. Galvanostatic Cycling Performance of SiO_xC in Sodium Half-Cells

After the investigation of the electrochemical processes allowing the Na^+ storage within our anode, the SiO_xC electrode is galvanostatically cycled in sodium half-cells using the TE-F electrolyte, as reported in Figure 4. Figure 4a,b shows selected voltage profiles from a test performed at 0.05 A g^{-1}, while the corresponding charge capacity vs cycle number and efficiency trends are displayed in Figure 4c,d. The first (dis)charge runs reported as insets in Figure 4a,b indicate initial low Coulombic efficiency of SiO_xC (53 and 51% using Al and Cu, respectively), due to the above-mentioned partial reduction of the electrolyte with SEI film formation, occurring between 1.2 and 0.2 V, in good agreement with the CV tests. Subsequently, the voltage profiles show a reversible process centered at an average value of 0.4 V, where the multiple peaks described upon CV appear merged into four sloping regions for both the Al and Cu current collectors, i.e., 1.2−0.8 V (∼15 and 20 mAh g^{-1} capacity contribution), 0.8−0.5 V (25 and 35 mAh g^{-1}), 0.5−0.1 V (40 and 55 mAh g^{-1}), and below 0.1 V (20 and 50 mAh g^{-1}), thus leading to an overall discharge capacity of 102 and 163 mAh g^{-1}, respectively. It is worth mentioning that charge and discharge occur with almost symmetrical profiles, with minor polarization and reversible shape, as also demonstrated by the corresponding capacity and efficiency trends displayed in Figure 4c,d. Therefore, the cells retain the initial capacity of 100 and 160 mAh g^{-1} over 400 galvanostatic cycles for 92.7% and 93.7%, while the average Coulombic efficiencies after the initial cycle are 99.4−99.5%, respectively, for the Al and Cu current collectors. These data remark on a notable reversibility and stability of the above-mentioned electrochemical processes and the relevant ability of the SiO_xC electrode for Na^+ storage.

With the aim of unraveling the contribution of the various components to SiO_xC capacity, blank electrodes of SiO_2, AC, and FLG cast on Cu are used as active material in Na half-cells (see Figure S4 in Supporting Information). Hence, the electrochemical performances of the Na|TE-F|SiO_2, Na|TE-F|FLG, and Na|TE-F|AC coin cells are investigated at a current of 0.05 A g^{-1} for 400 cycles, within the 0.01−2.0 V voltage range, similarly to the condition adopted for the SiO_xC anode. The results are depicted in Figure S4a in terms of charge capacity trend vs cycle number and voltage profiles at the first and 400th in Figure S4b. The data reported in Figure S4a evidence an initial charge (reversible) capacity of 13, 110, and 180 mAh g^{-1} for SiO_2, FLG, and AC, with capacity retention of 83.5%, 92.4%, and 89.2%, respectively. It is worth noting that the electrochemical process of AC is centered around 0.2 V, and the FLG electrode works around 0.8 V, while SiO_2 has a negligible sloping contribution (Figure S4b). On the other hand, the galvanostatic cycling of SiO_xC on Cu using the same experimental constraints (see Figure 4b,d) shows an initial charge capacity of 163.5 mAh g^{-1}, retained at 93.7% after 400 cycles. Therefore, we may state that the principal contributions to the electrode capacity are those of AC and FLG; instead, the SiO_2 principally leads to an increase of the electrode stability and cycle life in the Na cell due to a synergic interaction with the carbons and limited contribution to the overall capacity. Interestingly, taking into account the ratio of AC and FLG and SiO_2 in the electrode (55%, 26%, and 19%, respectively, from

Table 3. NLLS Analysis Carried Out on the Nyquist Plots Displayed in Figure 2d[a]

cell condition	circuit $R_e(R_iQ_i)Q_w$	R_1 [Ω]	R_2 [Ω]	$R_I = \sum R_i$ [Ω]	χ^2
OCV	$R_e(R_1Q_1)Q_w$	14.8 ± 0.1	-	14.8 ± 0.1	3×10^{-5}
after 1 CV	$R_e(R_1Q_1)(R_2Q_2)Q_w$	4.2 ± 0.1	3.8 ± 1.6	8.0 ± 1.6	3×10^{-5}
after 5 CV	$R_e(R_1Q_1)(R_2Q_2)Q_w$	7.1 ± 0.1	2.7 ± 1.0	9.8 ± 1.0	4×10^{-5}
after 10 CV	$R_e(R_1Q_1)(R_2Q_2)Q_w$	9.6 ± 0.1	2.5 ± 1.1	12.1 ± 1.1	7×10^{-5}

[a]The impedance spectra were acquired on a Na|TE-F|SiO_xC cell, having the positive electrode cast onto Cu, at the OCV and after 1, 5, and 10 CV runs, and fitted using the Boukamp software by exclusively accepting results with χ^2 values of the order of 10^{-5} or lower.

https://doi.org/10.1021/acs.energyfuels.5c06312
Energy Fuels 2026, 40, 3408−3422

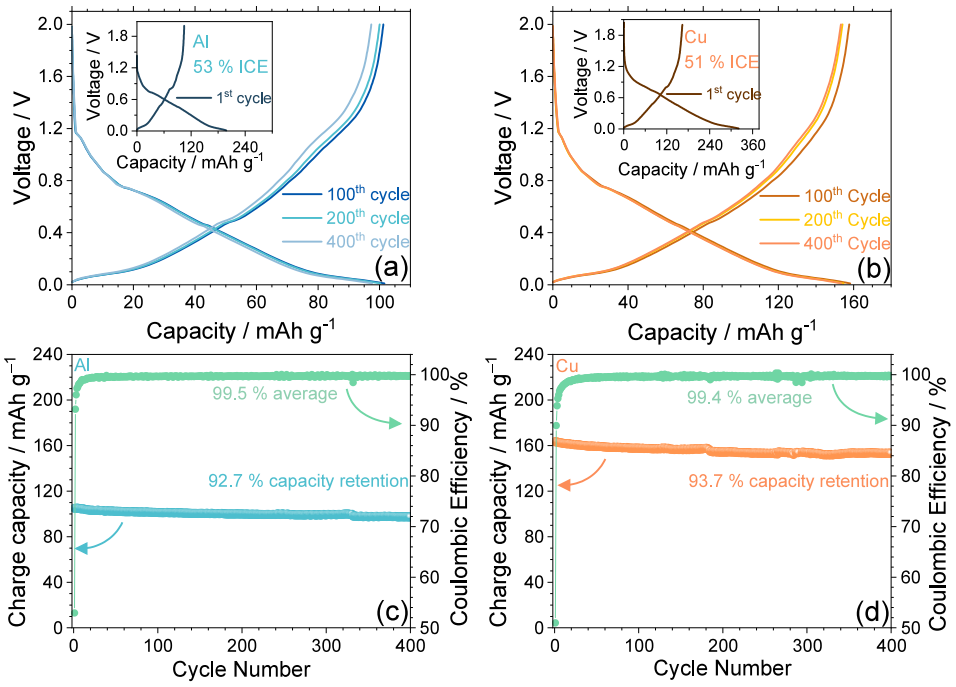

Figure 4. Galvanostatic cycling performance of Na|TE-F|SiO_xC half-cells with electrodes cast onto Al (light blue) or Cu (orange), respectively in terms of (a,b) selected voltage profiles (insets report the first discharge/charge run) and (c,d) corresponding charge capacity trends vs cycle number (Coulombic efficiency in right-hand side *y*-axes), voltage range: 0.01−2.0 V, current rate: 0.05 A g^{-1}; electrodes geometric area: 1.54 cm^2, loading: 2.3 ± 0.1 mg_{SiOxC} cm^{-2} (Al), 2.0 ± 0.1 mg_{SiOxC} cm^{-2} (Cu). The test was performed at 25 °C.

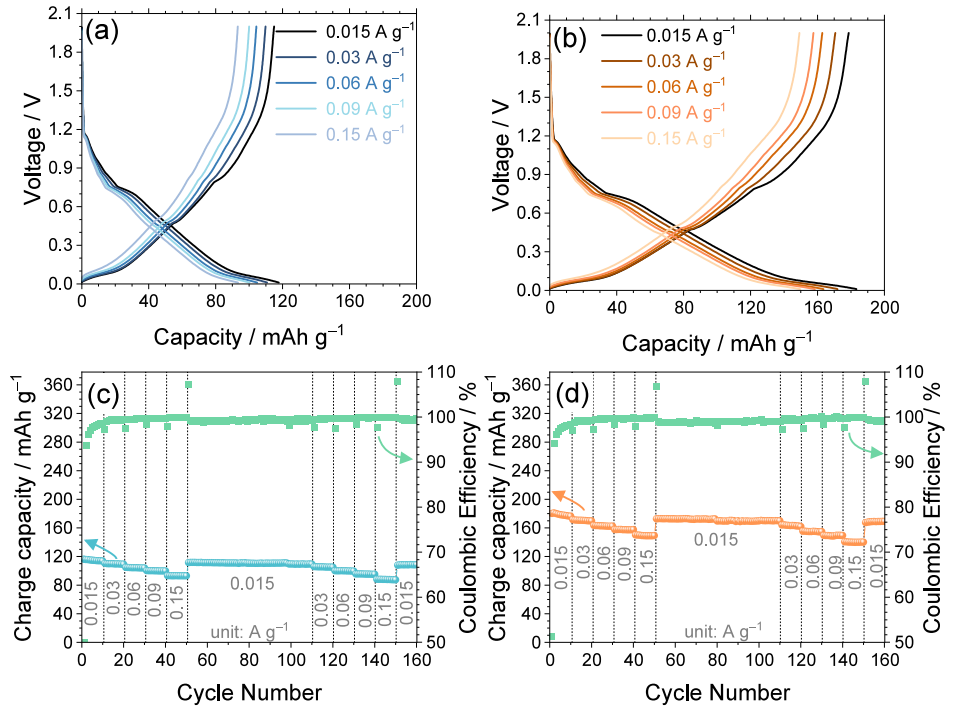

Figure 5. Galvanostatic cycling rate capability tests of Na|TE-F|SiO_xC half-cells, having electrodes cast either onto Al (blue) or Cu (orange), respectively in terms of (a,b) selected voltage profiles and (c,d) corresponding charge capacity trends vs cycle number (Coulombic efficiency in right-hand side *y*-axes), voltage range: 0.01−2.0 V, electrodes geometric area: 1.54 cm^2, loading: 2.3−2.5 mg_{SiOxC} cm^{-2}, temperature: 25 °C.

TGA in Figure 1b) and their initial reversible capacity (180, 110, and 13 mAh g^{-1}, respectively, from Figure S4), we may simply estimate an overall capacity around 130 mAh g^{-1}, which is lower than the reversible value actually achieved for SiO_xC on Cu (163.5 mAh g^{-1} in Figure 4d). The excess capacity may be attributed to the partial reduction of SiO_2 to SiO_x promoted by the synthesis environment (Ar/5% H_2) used to achieve the composite in this work (see Experimental Section for details).

Figure 5 shows further galvanostatic cycling tests of the SiO_xC in sodium half-cells, carried out by applying currents increasing every 10 cycles to determine the rate capability of the material. The selected voltage profiles (10th for each

https://doi.org/10.1021/acs.energyfuels.5c06312
Energy Fuels 2026, 40, 3408−3422

current rate) are reported in Figure 5a,b, and the corresponding charge capacity trend vs cycle number with Coulombic efficiency is displayed in Figure 5c,d, which show the applied current as insets. The voltage profiles reveal at the 10th cycle (Figure 5a,b) the electrochemical process centered at ∼0.45 V with more relevant specific capacity for electrodes cast on Cu rather than Al, as previously justified. On the other hand, the cells show higher capacity at the lower current of 0.015 A g^{-1} both for material cast on Al and on Cu (115 and 180 mAh g^{-1}, respectively) than at the higher one of 0.15 A g^{-1} (80 and 150 mAh g^{-1}, respectively), with a Coulombic efficiency of 98.4% at the lower current and 99.8% at the higher one. Thus, we can declare that the practical 1 C rate of the SiO_xC electrode cast onto Cu is 0.15 A g^{-1}. The higher capacity at the lower current is associated with the lower ohmic polarization that favors the occurrence of the electrochemical process, particularly at low voltage, while the higher efficiency at the higher current is typically ascribed to the kinetic limitation of side reactions such as electrolyte decomposition.[61] Hence, the delivered capacity decreases as current and polarization increase, and the Coulombic efficiency rises, while the pristine capacity values are restored as the current is lowered back to the lowest value upon 40 cycles. The delivered capacity and efficiency for each current of the SiO_xC electrode cast on Al and Cu are summarized in Table 4. After the above rate capability test, the cells hold their capacity for 110 cycles at 0.015 A g^{-1} and reveal almost the same behavior when the test is repeated, thus accounting for the remarkable stability of the SiO_xC material upon the stress induced by continuously increasing the current.

Table 4. Charge (Reversible) Capacity and Coulombic Efficiency for the 10th Cycle at the Various Currents of the Rate Capability Tests of Na\|TE-F\|SiO_xC Half-Cells in Figure 5

	Al current collector		Cu current collector	
current rate [A g^{-1}]	charge capacity [mAh g^{-1}]	Coulombic efficiency [%]	charge capacity [mAh g^{-1}]	Coulombic efficiency [%]
0.015	113.803	98.400	176.45	98.315
0.030	109.316	99.379	169.818	99.258
0.060	104.07	99.646	162.532	99.674
0.090	99.867	99.766	157.674	99.798
0.150	93.072	99.842	149.339	99.918

Overall, our results show that the SiO_xC anode has suitable performance both when cast on Cu or Al current collectors, particularly in terms of capacity retention. Despite ∼36% lower capacity, the latter current collector is considered the best candidate for full-cell application since it is lighter, less expensive, and therefore technically advantageous in terms of practical energy density and cost. Furthermore, the good electrochemical performance suggests the SiO_xC as a stable anode that favorably stores Na^+ through various processes. On the other hand, the anode synthesis is environmentally compatible since it involves solvents such as alcohol and H_2O and easily accessible materials (SiO_2, sucrose, and FLG) with a ratio optimized to avoid inactive fractions and increase the electrode conductivity.[39] However, the good electrochemical performances of SiO_xC in Na half-cells operating until 2 V using the TE-F electrolyte can be hindered in the Na-ion full-cell, which instead operates until higher voltage. Previous work has in fact indicated an electrochemical stability window of the TE-F electrolyte extended up to 2.98 V vs Na^+/Na before ongoing oxidative decomposition, which is an inconveniently low value to enable practical application.[62] This issue is limited in the subsequent paragraph by improving the electrode/electrolyte interphase through using different glyme-based electrolytes and adopting a chemical treatment of the SiO_xC electrode to compensate for the initial low-Coulombic efficiency of the anode.

3.4. Na-Ion Full-Cell Using the SiO_xC Anode

With the aim of further exploiting the potentiality of our anode, we designed a SIB configuration exploiting the SiO_xC material cast on Al with a layered oxide NCAM electrode operating at conveniently high potential, with outcomes reported in Figure 6. Since the TE-F electrolyte cannot withstand voltages higher than 3.8 V, we have replaced the electrolyte by using a shorter glyme (DEGDME) and a different salt ($NaPF_6$) to achieve the DE-P, which is stable until a suitable threshold.[63] Moreover, the PF_6^- anion possesses the lowest HOMO energy level among other salts,[57−59] making it more stable toward electron loss and/or decomposition. Prior to the full-cell study, the electrochemical performance of the SiO_xC electrode is investigated either by CV/EIS or galvanostatic cycling using the DE-P electrolyte, and the results are reported in Figure S5 and Table S4 (Supporting Information). The CV curves suggest a faster kinetic when using DEGDME than TEGDME, which is indicated by an almost three-fold increase of peak currents in DE-P (Figure S5a) compared to TE-F (Figure 3a), both during cathodic and anodic scans. The EIS spectra reported in terms of the Nyquist plot (see Figure S5b and related NLLS fitting in Table S4) indicate an almost blocking electrode−electrolyte interphase with adequately conductive character, demonstrated by almost 1 order of magnitude of lower resistance in DE-P than TE-F (compare with Figure 3c). These results suggest enhanced film-forming properties of PF_6^- and possible suppression of Al^{3+} dissolution, since the electrolyte bulk resistance remains stable in Figure S5b. Instead, the results reported in Figure 3c suggest that some Al^{3+} can be dissolved in the TE-F electrolyte, as highlighted by the different *x*-axis intercept upon the OCV in the corresponding Nyquist plots that alters the bulk resistance. The galvanostatic cycling performance of SiO_xC using the DE-P electrolyte is investigated by running a current rate capability test, and the results are displayed in Figure S5c in terms of charge capacity trend vs the cycle number and in Figure S5d in terms of selected voltage profiles. The lowered interphase resistance in DE-P compared to TE-F electrolyte enhances the rate capability and allows the SiO_xC electrode to deliver 5−10 mAh g^{-1} more capacity at the same current rate (compare Figures S5c,d with 5a,c). Subsequently, the SiO_xC anode is used in a Na-ion full-cell with the DE-P and the Na-deficient NCAM cathode. The latter can in fact deliver a capacity of 50 mAh g^{-1} during the first charge in the Na half-cell and a higher value of 122 mAh g^{-1} during discharge, as reported in Figure S6. Prior to full-cell assembling, the SiO_xC anode has been activated by chemical capillary contact with Na metal for 3 min to achieve a sodiation degree suitable for compensating the cathode Na-deficiency, as demonstrated by the galvanostatic cycle of the resulting Na-SiO_xC electrode in the half-cell in Figure S6.[43] The chemical presodiation of the anode performed mechanically outside the full-cell leads to its

https://doi.org/10.1021/acs.energyfuels.5c06312
Energy Fuels 2026, 40, 3408−3422

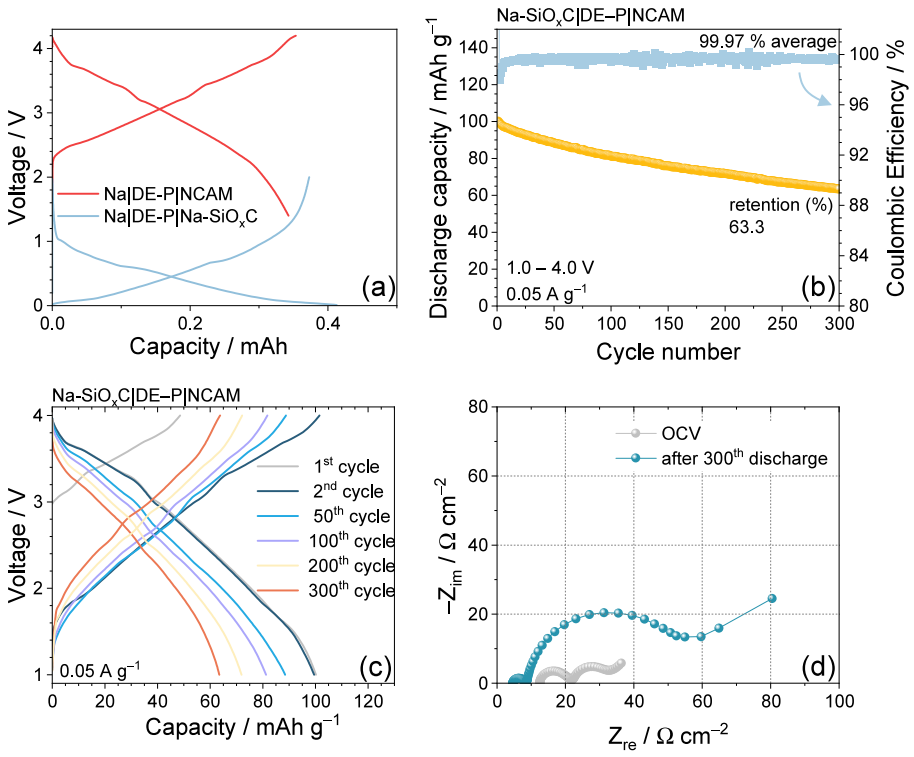

Figure 6. (a) Reversible voltage profiles at the steady-state of SiO_xC from 2 to 0.01 V (light blue) and NCAM from 1.4 to 4.2 V (red) in the Na half-cell, performed at 0.05 A g^{-1} to analyze the voltage−capacity curve evolution; (b,c) galvanostatic cycling performance of the Na-SiO_xC|DE-P|NCAM full-cell, in detail: (b) discharge capacity trends vs cycle number (Coulombic efficiency in right-hand side *y*-axis); (c) selected voltage profiles; (d) Nyquist plots recorded by EIS related to the full-cell, with EIS performed at the OCV cell condition and at the discharge state after the 300th cycle, between 500 kHz and 20 mHz; alternate voltage signal: 10 mV. Galvanostatic cycling was carried out using a current rate of 0.05 A g^{-1} in the 1.0−4.0 V voltage range, with active material content: 5.9 ± 0.1 mg_{NCAM} cm^{-2} and 6.2 ± 0.1 mg_{SiO_xC} cm^{-2}, both electrodes cast onto Al, geometric area: 1.54 cm^2. Temperature: 25 °C.

Table 5. NLLS Analysis Carried Out on the Nyquist Plots Displayed in Figure 6d[a]

cell condition	circuit $R_e(R_1Q_1)Q_w$	R_1 [Ω]	R_2 [Ω]	R_2 [Ω]	χ^2
OCV	$R_e(R_1Q_1)(R_2Q_2)Q_w$	12.6 ± 0.5	18.8 ± 1.0	31.4 ± 1.1	1×10^{-4}
after 300 cycles	$R_e(R_1Q_1)(R_2Q_2)Q_w$	5.7 ± 0.2	60 ± 5.1	65.7 ± 5.1	2×10^{-4}

[a]Impedance spectra acquired on a Na|TE-F|SiO_xC cell at the OCV and after 300 (dis)charge runs and fitted using the Boukamp software by exclusively accepting results with χ^2 values of the order of 10^{-4}.

balancing with a N/P ratio approaching 1, as evidenced by the voltage profiles of the two electrodes separately tested in Na half-cells in Figure S6. The capacities well match each other, thus enabling a stable full-cell if the active materials are balanced to about 1 to 1 with respect to their weight, as evidenced by steady-state voltage profiles reported separately for the anode and cathode in Figure 6a. Subsequently, the Na-SiO_xC|DE-P|NCAM full-cell is cycled at 0.05 A g^{-1} in the 1.0−4.0 V range. The full-cell displays adequate stability and electrochemical response upon cycling (Figure 6b), highlighted by a first discharge capacity of 100.2 mAh g^{-1}, retained at 63.3% after 300 cycles, and a mean Coulombic efficiency corresponding to 99.97%, allowed by the highly reversible electrochemical activity of SiO_xC.

The voltage profile evolution upon cycling of this cell (Figure 6c) suggests the combination of the anode and cathode signatures, with an average working voltage centered at about 2.9 V, and almost symmetrical profiles that ensure adequate energy efficiency of this SIB. After the first cycle, the capacity is maintained at 100.2 mAh g^{-1} and then slowly decreases to 88.5 at the 50th cycle, steadily losing on average 0.123 mAh g^{-1} each cycle (Figure 6b). This trend indicates that the cell operates properly thanks to N/P optimization (around 1.1), while the relatively stable cycling is promoted by both the anode and cathode optimal electrochemical responses. The Coulombic efficiency of the cell (Figure 6b) shows a steady-state value ranging from 99.4% to 100.1%, thus further accounting for the suitability of the anode material we developed herein. The use of the chemical activation of the anode (i.e., chemical presodiation by capillary contact) developed in a previous work allows possible scalability of the full-cell, without any electrochemical pretreatment, which is a remarkable advantage in view of a practical application of the battery.[43] The interphase resistance evolution was tracked by acquiring EIS spectra at the OCV condition and at the end of the 300th discharge. The obtained Nyquist plots are reported in Figure 6d, and their NLLS analysis is displayed in Table 5, which suggests a good stability of the interphase, with resistance incrementing from 31.4 Ω at the OCV to only 65.7 Ω at the end of the galvanostatic cycling test. Notwithstanding the substantial stability of the bulk resistance when DE-P electrolyte is used (see Figure S5), the bulk resistance of the

https://doi.org/10.1021/acs.energyfuels.5c06312
Energy Fuels 2026, 40, 3408−3422

full-cell still changes. This outcome could result from some transition-metal dissolution from NCAM, as well as slight changes in the cell constant due to evolution of the electrode structure upon cycling, such as SEI formation/dissolution and cointercalation phenomena at both electrodes.

The reasons for the good electrochemical features of the full-cell are further investigated by checking the features of the SiO_xC electrode upon cycling. Figure 7 displays the structural

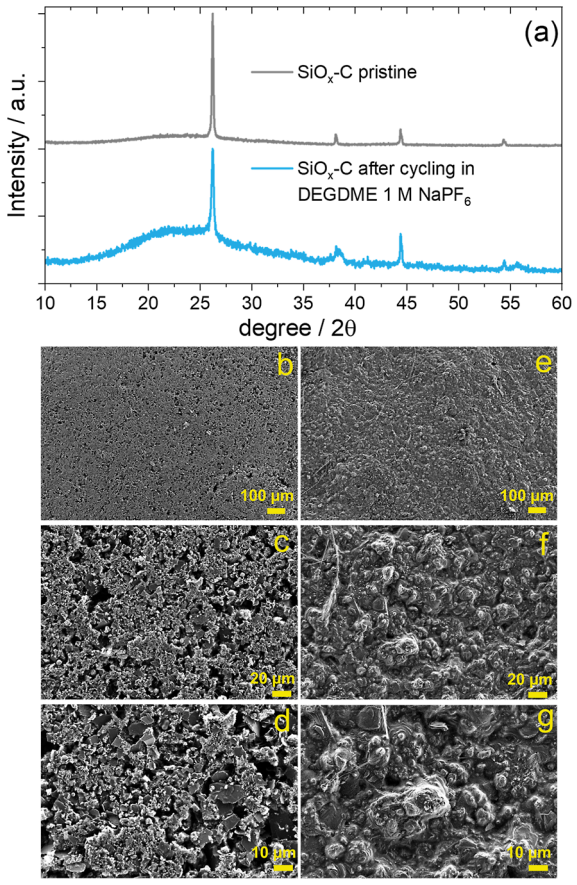

Figure 7. Structural and morphological characterization of the SiO_xC electrode upon cycling: (a) X-ray diffractograms for either the pristine or cycled SiO_xC electrode and (b–g) SEM images acquired in secondary electron mode reporting the (b–d) pristine and (e–g) cycled SiO_xC electrodes in a Na half-cell using the DE-P electrolyte for 100 cycles (electrode recovered at the fully desodiated state).

and morphological investigation of either a pristine or cycled electrode using the DE-P electrolyte (100 cycles in half-cell, electrode recovered at the fully desodiated state). The XRD patterns reported in Figure 7a suggest that the crystalline structure is retained after galvanostatic cycling, despite the broadening of the peaks at 2θ = 38.2° and the intensity increase of the one at 2θ = 44.4°. Generally, an increase of the baseline signal is observed, indicating the formation of SEI on the electrode surface, while the graphite (002) plane reflection appears fully retained. The morphology of the SiO_xC electrode is displayed in Figure 7b–g, which reports two sets of 3 panels, (b, c, d) and (e, f, g), depicting, respectively, the pristine and cycled electrodes. Overall, the uniform smooth surface achieved through the electrode casting process reflects the SEI formation after galvanostatic cycling (Figure 7e–g) that crumples the surface, but without relevant signs of cracking, fracturing, or deterioration, thus supporting the enhanced stability demonstrated by the cells.

Hereafter, the performances of our SiO_xC material are compared with other substrates reported in literature studies for application in SIBs. Among the carbon sources, we considered sucrose since it represents the most widely available and adopted nongraphitizable compound and, most importantly, represents the same feedstock we exploited in this work, as well as the silicon oxide, which is an abundant material in the earth's crust. Table S6 (Supporting Information) summarizes this comparison in terms of the anode voltage window, charge/discharge current density, reversible capacity, cycle number, and actual application in a full Na-ion battery. Accordingly, precarbonization has been adopted for regulating sucrose-based hard carbon pore structure for SIB anodes, and the material delivered in the Na half-cell a capacity of 374 mAh g^{-1} for 150 cycles.[64] A sucrose–anthracite composite supplemented by a KOH/HCl washing strategy has been proposed as an anode material for SIBs, operating in Na half-cells within the 0.0–2.5 V range with a maximum capacity of 302 mAh g^{-1} deducted from a rate capability test.[65] Furthermore, tuning the porosity of hard carbons elaborated from sucrose has led to an anode material operating from 0.01 to 2.75 V in half-cells with a capacity of 246 mAh g^{-1} achieved by a rate capability test.[66] Spherical sucrose-derived hard carbon with closed pores achieved via amino-aldehyde condensation delivered in the 0.0–2.0 V range a capacity of 313 mAh g^{-1} in Na half-cells.[67] A carbon inverse opal macroporous monolithic structure has been exploited as an electrode for SIBs, within a voltage ranging from 0.014 to 2.0 V in Na cells with a capacity of 40 mAh g^{-1} for 250 cycles.[68] Hard carbon microspheres have been proposed as anode material for SIBs delivering in half-cells within the 0.005–1.5 V range a relevant capacity of 385 mAh g^{-1} for 50 cycles.[69] Despite part of these materials delivered a higher capacity than the SiO_xC electrode (i.e., 183 mAh g^{-1}) in half-cells, they have depicted a lower cycle life (i.e., a maximum value of 250 compared to 400 cycles). More importantly, none of the cited materials demonstrated the practical application in a full Na-ion cell that typically requires high loadings and low irreversible capacity during the initial cycle, which is achieved in our work by the capillary-contact chemical sodiation pathway of the anode. Application in full Na-ion cells has been demonstrated by recent work using amorphous monodispersed hard carbon microspherules derived from biomass as an anode operating in the 0.0–3.0 V range with a capacity of 311 mAh g^{-1} over 100 cycles, and the full-cell exploited the $Na_{2/3}Ni_{1/3}Mn_{2/3}O_2$ cathode at 3 V average working voltage with a retention of about 70% for 140 cycles.[70] Another hard carbon with a manipulated micropore structure has been exploited between 0.01 and 2.5 V, with a capacity of 315 mAh g^{-1} achieved by a rate capability test, and used in a SIB with a $Na_{0.67}Ni_{0.28}Zn_{0.05}Mn_{0.62}Ti_{0.05}O_2$ (NNZMTO) cathode over 200 cycles with a retention slightly higher than 80% and an average voltage of 3.3 V.[71] Finally, a SiO_2-based anode operating in the 0.01–3.0 V range with a capacity of 180 mAh g^{-1} for 50 cycles has been exploited in a full-cell using a $Na_3V_2(PO_4)_3$ cathode with an optimized N/P ratio, delivering an average voltage of 3 V about 100 mAh g^{-1} for 50 cycles.[32]

4. CONCLUSION

A SiO_xC electrode has been achieved from SiO_2, FLG, and sucrose by hydrothermal treatment and exposure to Ar/H_2

https://doi.org/10.1021/acs.energyfuels.5c06312
Energy Fuels 2026, 40, 3408–3422

flow inside a furnace for application in SIB. TGA revealed an overall C-to-SiO_x weight ratio of 81% to 19% and FLG-to-AC ratio of 55% to 26%. FT-IR suggested the presence of various functional groups in SiO_xC, such as C−OH, Si−O−CO−O−, Si−O−, −SiOH, −CH, −C−O−CO−O−, −C═C−, and C−O−, originating from the formulation of the precursors and promoted by the synthetic pathway. The presence of these functionalities has been indicated to promote the electrochemical performance of the anode; however, it possibly increases irreversible reactions. SEM/TEM indicated the SiO_xC has an array in which FLG, AC, and SiO_x are mixed within an extended submicron matrix as well as 3D aggregates of the same nature. The CV response of the SiO_xC electrode in the Na cell revealed multiple processes, including initial reductive decomposition with SEI formation from 1.3 to 0.3 V vs Na^+/Na, reversible Na^+-solvent cointercalation from 1.3 to 0.7 V, Na^+ intercalation at 0.45 V, Na^+ insertion or deposition in AC nearby 0 V, and minor Na−Si alloying at about 0.05 V vs Na^+/Na. The SiO_xC depicted in the half-cell charge and discharge occurring with an almost symmetrical profile for both Al and Cu current collectors, with a capacity of 102 and 163 mAh g^{-1} retained over 400 cycles for 93% and 94%, respectively, and Coulombic efficiencies higher than 99% after the initial cycles. On the other hand, the tests demonstrated that the main contributions to the electrode capacity were those of AC and FLG, while SiO_2 has principally led to the increase of the stability and cycle life due to its synergic interaction with the carbons and only marginally to the overall capacity. The SiO_xC cast on Al and on Cu revealed a capacity ranging from 115 and 180 mAh g^{-1} at 0.015 A g^{-1} to 80 and 150 mAh g^{-1} at 0.15 A g^{-1}. Despite 36% lower capacity for electrodes cast on Al, this current collector has been considered the most suitable candidate for full-cell application since it is lighter, cheaper, and therefore advantageous in terms of cell practical energy density and cost. Before the use in full-cell, the SiO_xC electrode was activated through chemical capillary contact treatment to achieve a Na-SiO_xC anode for SIBs. The full-cell combining the anode with a NCAM cathode utilized a DE-P electrolyte characterized by adequate anodic stability to exploit the layered material. Hence, the Na-SiO_xC|DE-P|NCAM full-cell had an average working voltage centered at about 2.9 V, with capacity ranging from 100 mAh g^{-1} to 63 mAh g^{-1} upon 300 cycles and average Coulombic efficiency exceeding 99.9%. A higher capacity can possibly be achieved from this full-cell by further tuning the cell balance (increasing the N/P ratio to get an adequate Na reservoir) or by incrementing the furnace step temperature, which is expected to enhance the specific capacity of the anode. These data suggest a possible setup of the Na-ion full-cell using the SiO_xC anode, glyme-based Na electrolyte, and NCAM cathode in view of the complementary application of SIB technology with LIBs.

■ ASSOCIATED CONTENT

Supporting Information

The Supporting Information is available free of charge at https://pubs.acs.org/doi/10.1021/acs.energyfuels.5c06312.

XPS survey spectrum of the SiO_xC powder; additional morphological characterization of SiO_xC through SEM and TEM; electrochemical characterization of SiO_xC components: FLG, AC, and SiO_2; cycling performances of the SiO_xC components cast on Cu in the Na cell; electrochemical characteristics of the SiO_xC cast on Al in the Na half-cell using the diglyme electrolyte; electrochemical response of NCAM and SiO_xC (chemically sodiated) cast on Al in the Na half-cell; and comparison of this work with literature studies adopting either sucrose as a carbon source or SiO_2 (PDF)

■ AUTHOR INFORMATION

Corresponding Author

Josef Hassoun − *University of Ferrara, Department of Chemical, Pharmaceutical and Agricultural Sciences, 44121 Ferrara, Italy; Center for Nanotechnology Innovation @ NEST, Istituto Italiano di Tecnologia, I-56127 Pisa, Italy;* orcid.org/0000-0002-8218-5680; Email: josef.hassoun@unife.it, josef.hassoun@iit.it

Authors

Edoardo Barcaro − *University of Ferrara, Department of Chemical, Pharmaceutical and Agricultural Sciences, 44121 Ferrara, Italy*

Daniel Amato − *University of Ferrara, Department of Chemical, Pharmaceutical and Agricultural Sciences, 44121 Ferrara, Italy*

Stiven Forti − *Center for Nanotechnology Innovation @ NEST, Istituto Italiano di Tecnologia, I-56127 Pisa, Italy;* orcid.org/0000-0002-8939-3175

Camilla Coletti − *Center for Nanotechnology Innovation @ NEST, Istituto Italiano di Tecnologia, I-56127 Pisa, Italy;* orcid.org/0000-0002-8134-7633

Complete contact information is available at: https://pubs.acs.org/10.1021/acs.energyfuels.5c06312

Notes

The authors declare no competing financial interest.

■ ACKNOWLEDGMENTS

The project is funded under the National Recovery and Resilience Plan (NRRP), Mission 04 Component 2 Investment 1.5—NextGenerationEU, Call for tender no. 3277 dated 30/12/2021, Award Number: 0001052 dated 23/06/2022. The authors also thank the grant "Fondo di Ateneo per la Ricerca Scientifica, FAR 2024" from the University of Ferrara and the project "Accordo di Collaborazione Quadro 2015" between the University of Ferrara (Department of Chemical and Pharmaceutical Sciences) and Sapienza University of Rome (Department of Chemistry). The company BeDimensional S.p.A. (Lungotorrente Secca 30R, Genova, 16163, Italy) is acknowledged for kindly providing FLG powder employed as a component of SiO_xC.

■ REFERENCES

(1) Titirici, M.; Johansson, P.; Crespo Ribadeneyra, M.; Au, H.; Innocenti, A.; Passerini, S.; Petavratzi, E.; Lusty, P.; Tidblad, A. A.; Naylor, A. J.; Younesi, R.; Chart, Y. A.; Aspinall, J.; Pasta, M.; Orive, J.; Babulal, L. M.; Reynaud, M.; Latham, K. G.; Hosaka, T.; Komaba, S.; Bitenc, J.; Ponrouch, A.; Zhang, H.; Armand, M.; Kerr, R.; Howlett, P. C.; Forsyth, M.; Brown, J.; Grimaud, A.; Vilkman, M.; Dermenci, K. B.; Mousavihashemi, S.; Berecibar, M.; Marshall, J. E.; McElroy, C. R.; Kendrick, E.; Safdar, T.; Huang, C.; Zanotto, F. M.; Troncoso, J. F.; Dominguez, D. Z.; Alabdali, M.; Vijay, U.; Franco, A. A.; Pazhaniswamy, S.; Grant, P. S.; López Guzman, S.; Fehse, M.;

Galceran, M.; Antuñano, N. 2024 Roadmap for Sustainable Batteries. *J. Phys.: Energy* **2024**, *6* (4), 041502.
(2) Scrosati, B. Lithium Rocking Chair Batteries: An Old Concept? *J. Electrochem. Soc.* **1992**, *139* (10), 2776−2781.
(3) Yabuuchi, N.; Kubota, K.; Dahbi, M.; Komaba, S. Research Development on Sodium-Ion Batteries. *Chem. Rev.* **2014**, *114* (23), 11636−11682.
(4) Liu, Q.; Hu, Z.; Chen, M.; Zou, C.; Jin, H.; Wang, S.; Chou, S.; Liu, Y.; Dou, S. The Cathode Choice for Commercialization of Sodium-Ion Batteries: Layered Transition Metal Oxides versus Prussian Blue Analogs. *Adv. Funct. Mater.* **2020**, *30* (14), 1909530.
(5) Li, A.-M.; Zavalij, P. Y.; Omenya, F.; Li, X.; Wang, C. Salt-in-Presalt Electrolyte Solutions for High-Potential Non-Aqueous Sodium Metal Batteries. *Nat. Nanotechnol.* **2025**, *20*, 388−396.
(6) Buchholz, D.; Vaalma, C.; Chagas, L. G.; Passerini, S. Mg-Doping for Improved Long-Term Cyclability of Layered Na-Ion Cathode Materials - The Example of P2-Type $Na_xMg_{0.11}Mn_{0.89}O_2$. *J. Power Sources* **2015**, *282*, 581−585.
(7) Yu, T.-Y.; Hwang, J.-Y.; Bae, I. T.; Jung, H.-G.; Sun, Y.-K. High-Performance Ti-Doped O3-Type $Na[Ti_x(Ni_{0.6}Co_{0.2}Mn_{0.2})_{1-x}]O_2$ Cathodes for Practical Sodium-Ion Batteries. *J. Power Sources* **2019**, *422*, 1−8.
(8) Di Lecce, D.; Campanella, D.; Hassoun, J. Insight on the Enhanced Reversibility of a Multimetal Layered Oxide for Sodium-Ion Battery. *J. Phys. Chem. C* **2018**, *122* (42), 23925−23933.
(9) Hasa, I.; Passerini, S.; Hassoun, J. Toward High Energy Density Cathode Materials for Sodium-Ion Batteries: Investigating the Beneficial Effect of Aluminum Doping on the P2-Type Structure. *J. Mater. Chem. A Mater.* **2017**, *5* (9), 4467−4477.
(10) Marangon, V.; Bischof, K.; Regalado, A. A.; Keppeler, M.; Pogosova, M.; Wan, M.; Choi, J.; Fleischmann, S.; Diemant, T.; Wohlfahrt-Mehrens, M.; Hölzle, M.; Waldmann, T.; Bresser, D. Cell Design and Chemistry of Commercial Sodium-Ion Battery Cells. *J. Power Sources* **2025**, *634*, 236496.
(11) Dahbi, M.; Yabuuchi, N.; Kubota, K.; Tokiwa, K.; Komaba, S. Negative Electrodes for Na-Ion Batteries. *Phys. Chem. Chem. Phys.* **2014**, *16* (29), 15007.
(12) Dou, X.; Hasa, I.; Saurel, D.; Vaalma, C.; Wu, L.; Buchholz, D.; Bresser, D.; Komaba, S.; Passerini, S. Hard Carbons for Sodium-Ion Batteries: Structure, Analysis, Sustainability, and Electrochemistry. *Mater. Today* **2019**, *23*, 87−104.
(13) Fang, S.; Bresser, D.; Passerini, S. Transition Metal Oxide Anodes for Electrochemical Energy Storage in Lithium- and Sodium-Ion Batteries. *Adv. Energy Mater.* **2020**, *10* (1), 1902485.
(14) Chen, Y.; Li, F.; Guo, Z.; Song, Z.; Lin, Y.; Lin, W.; Zheng, L.; Huang, Z.; Hong, Z.; Titirici, M.-M. Sustainable and Scalable Fabrication of High-Performance Hard Carbon Anode for Na-Ion Battery. *J. Power Sources* **2023**, *557*, 232534.
(15) Leng, Y.; Dong, S.; Chen, Z.; Sun, Y.; Xu, Q.; Ma, L.; He, X.; Hai, C.; Zhou, Y. Preparation of High-Performance Anode Materials for Sodium-Ion Batteries Using Bamboo Waste: Achieving Resource Recycling. *J. Power Sources* **2024**, *613*, 234826.
(16) Yang, B.; Wang, J.; Zhu, Y.; Ji, K.; Wang, C.; Ruan, D.; Xia, Y. Engineering Hard Carbon with High Initial Coulomb Efficiency for Practical Sodium-Ion Batteries. *J. Power Sources* **2021**, *492*, 229656.
(17) Zhu, H.; Shen, F.; Luo, W.; Zhu, S.; Zhao, M.; Natarajan, B.; Dai, J.; Zhou, L.; Ji, X.; Yassar, R. S.; Li, T.; Hu, L. Low Temperature Carbonization of Cellulose Nanocrystals for High Performance Carbon Anode of Sodium-Ion Batteries. *Nano Energy* **2017**, *33*, 37−44.
(18) Xie, L.; Tang, C.; Bi, Z.; Song, M.; Fan, Y.; Yan, C.; Li, X.; Su, F.; Zhang, Q.; Chen, C. Hard Carbon Anodes for Next-Generation Li-Ion Batteries: Review and Perspective. *Adv. Energy Mater.* **2021**, *11* (38), 2101650.
(19) Adam, M.; Abdalla, T.; Mohammed, M.; Bari, M. A. A.; Hossain, M. M. Fabrication, Characterization, and Applications of Hard Carbons: A Comprehensive Review. *J. Power Sources* **2025**, *652*, 237674.
(20) Gan, S.; Huang, Y.; Hong, N.; Zhang, Y.; Xiong, B.; Zheng, Z.; He, Z.; Gao, S.; Deng, W.; Zou, G.; Hou, H.; Ji, X. Comprehensive Understanding of Closed Pores in Hard Carbon Anode for High-Energy Sodium-Ion Batteries. *Nano-Micro Lett.* **2025**, *17* (1), 325.
(21) Xu, L.; Li, Y.; Xiang, Y.; Li, C.; Zhu, H.; Li, C.; Zou, G.; Hou, H.; Ji, X. Bridging Structure and Performance: Decoding Sodium Storage in Hard Carbon Anodes. *ACS Nano* **2025**, *19* (15), 14627−14651.
(22) Kim, H.; Hong, J.; Yoon, G.; Kim, H.; Park, K.-Y.; Park, M.-S.; Yoon, W.-S.; Kang, K. Sodium Intercalation Chemistry in Graphite. *Energy Environ. Sci.* **2015**, *8* (10), 2963−2969.
(23) Åvall, G.; A. Ferrero, G.; Janßen, K. A.; Exner, M.; Son, Y.; Adelhelm, P. In Situ Pore Formation in Graphite Through Solvent Co-Intercalation: A New Model for The Formation of Ternary Graphite Intercalation Compounds Bridging Batteries and Supercapacitors. *Adv. Energy Mater.* **2023**, *13* (38), 2301944.
(24) Son, Y.; Åvall, G.; Ferrero, G. A.; Freytag, A. I.; Escher, I.; Janßen, K. A.; Jauregui, M.; Saurel, D.; Galceran, M.; Adelhelm, P. Diglyme as a Promoter for the Electrochemical Formation of Quaternary Graphite Intercalation Compounds Containing Two Different Types of Solvents. *Batteries Supercaps* **2024**, *7* (3), No. e202300506.
(25) Moriwake, H.; Kuwabara, A.; Fisher, C. A. J.; Ikuhara, Y. Why Is Sodium-Intercalated Graphite Unstable? *RSC Adv.* **2017**, *7* (58), 36550−36554.
(26) Jache, B.; Adelhelm, P. Use of Graphite as a Highly Reversible Electrode with Superior Cycle Life for Sodium-Ion Batteries by Making Use of Co-Intercalation Phenomena. *Angew. Chem., Int. Ed.* **2014**, *53* (38), 10169−10173.
(27) Hasa, I.; Dou, X.; Buchholz, D.; Shao-Horn, Y.; Hassoun, J.; Passerini, S.; Scrosati, B. A Sodium-Ion Battery Exploiting Layered Oxide Cathode, Graphite Anode and Glyme-Based Electrolyte. *J. Power Sources* **2016**, *310*, 26−31.
(28) Jain, P. K. The Graphite Processing Sector: A Global Perspective on Practices, Applications, Trade, and Trends Toward 2047. *Miner. Process. Extr. Metall. Rev.* **2025**, 1−24.
(29) Liu, Z.; Yu, Q.; Zhao, Y.; He, R.; Xu, M.; Feng, S.; Li, S.; Zhou, L.; Mai, L. Silicon Oxides: A Promising Family of Anode Materials for Lithium-Ion Batteries. *Chem. Soc. Rev.* **2019**, *48* (1), 285−309.
(30) Yang, Z.; Zhang, H.; Jiang, R.; Cheng, X.; Jing, C.; Luo, J.; Jia, P.; Yang, J. Recent Progress on Boosting Initial Coulombic Efficiency of SiOx-Based Anode Materials for Lithium-Ion Batteries. *J. Energy Storage* **2025**, *135*, 118400.
(31) Chandra, C.; Devina, W.; Alvin, S.; Kim, J. New Strategy for Increasing Sodium-Ion Uptake in Silicon Oxycarbides. *Chem. Eng. J.* **2021**, *404*, 126520.
(32) Chuong, Y. N. K.; Le, P. M. L.; Vu, P. T.; Van Tran, M. Full-Cell C/SiO2||Na3V2(PO4)3 High-Performance Na-Ion Battery: Diffusion Kinetics and N/P Optimization. *Appl. Phys. A: Mater. Sci. Process.* **2024**, *130* (9), 633.
(33) Pustovalova, A. A.; Morozov, A. V.; Polivara, N. M.; Dikhtyar, Y. Y.; Nedoluzhko, A. I.; Pazhetnov, E. M.; Abakumov, A. M. The Role of Solvent during Solvothermal Synthesis of Amorphous SiOx Anode Materials for Advanced Li-Ion Batteries. *Mater. Res. Bull.* **2025**, *192*, 113613.
(34) Chen, T.; Yan, X.; Zhang, Y.; Cao, J.; Hu, L.; Gao, W.; Li, D.; Song, W.; Zhang, J.; Xia, Y.; Xia, X.; Zhang, W.; Huang, H. An Effective Strategy for Regulating SiO_x/Si Components by Thermal Reduction of Biomass Diatomite for Lithium-Ion Battery Anodes. *J. Energy Storage* **2025**, *138*, 118704.
(35) Luo, W.; Shi, Q.; Zhang, C.; Yi, R.; Zhao, W.; Cui, Y.; Shen, Y.; Ge, J.; Wang, C.; Huang, Y. SiO_x Enhances Prelithiation Kinetics and Homogeneity in Graphite-Based Anodes. *J. Mater. Chem. A Mater.* **2025**, *13* (40), 34640−34647.
(36) Qiao, Y.; He, Z.; Tian, S.; Song, C.; Zhang, F.; Xia, Y. Balancing Act: Optimizing SiO_x Specific Surface Area for Enhanced Cycling Stability and Rate Capability in Practical 350 Wh/kg Lithium-Ion Batteries. *J. Power Sources* **2025**, *649*, 237486.

https://doi.org/10.1021/acs.energyfuels.5c06312
Energy Fuels 2026, 40, 3408−3422

(37) Del Rio Castillo, A. E.; Pellegrini, V.; Ansaldo, A.; Ricciardella, F.; Sun, H.; Marasco, L.; Buha, J.; Dang, Z.; Gagliani, L.; Lago, E.; Curreli, N.; Gentiluomo, S.; Palazon, F.; Prato, M.; Oropesa-Nuñez, R.; Toth, P. S.; Mantero, E.; Crugliano, M.; Gamucci, A.; Tomadin, A.; Polini, M.; Bonaccorso, F. High-Yield Production of 2D Crystals by Wet-Jet Milling. *Mater. Horiz.* **2018**, *5* (5), 890−904.
(38) Barcaro, E.; Marangon, V.; Bresser, D.; Hassoun, J. Scalable Li-Ion Battery with Metal/Metal Oxide Sulfur Cathode and Lithiated Silicon Oxide/Carbon Anode. *ChemSusChem* **2025**, *18* (1), No. e202400615.
(39) Barcaro, E.; Marangon, V.; Mutarelli, M.; Hassoun, J. A Lithium-Ion Battery with Cycling Stability Promoted by the Progressive Activation of a Silicon Oxide Anode in Graphene-Amorphous Carbon Matrix. *J. Power Sources* **2024**, *595*, 234059.
(40) Bauer, A.; Song, J.; Vail, S.; Pan, W.; Barker, J.; Lu, Y. The Scale-up and Commercialization of Nonaqueous Na-Ion Battery Technologies. *Adv. Energy Mater.* **2018**, *8* (17), 1702869.
(41) Boukamp, B. A Package for Impedance/Admittance Data Analysis. *Solid State Ion* **1986**, *18*−*19*, 136−140.
(42) Boukamp, B. A Nonlinear Least Squares Fit Procedure for Analysis of Immittance Data of Electrochemical Systems. *Solid State Ion* **1986**, *20* (1), 31−44.
(43) Minnetti, L.; Barcaro, E.; Sbrascini, L.; Nobili, F.; Hassoun, J. Chemical Approach to Achieve Sodiated Alloying Anode for Direct Application in Na-Ion Battery. *Mater. Res. Bull.* **2025**, *191*, 113546.
(44) Moosavi-Nasab, M.; Taherian, A. R.; Bakhtiyari, M.; Farahnaky, A.; Askari, H. Structural and Rheological Properties of Succinoglycan Biogums Made from Low-Quality Date Syrup or Sucrose Using Agrobacterium Radiobacter Inoculation. *Food Bioprocess Technol.* **2012**, *5* (2), 638−647.
(45) Li, K.-M.; Jiang, J.-G.; Tian, S.-C.; Chen, X.-J.; Yan, F. Influence of Silica Types on Synthesis and Performance of Amine-Silica Hybrid Materials Used for CO_2 Capture. *J. Phys. Chem. C* **2014**, *118* (5), 2454−2462.
(46) Freda, M.; Piluso, A.; Santucci, A.; Sassi, P. Transmittance Fourier Transform Infrared Spectra of Liquid Water in the Whole Mid-Infrared Region: Temperature Dependence and Structural Analysis. *Appl. Spectrosc.* **2005**, *59* (9), 1155−1159.
(47) Danon, A.; Stair, P. C.; Weitz, E. FTIR Study of CO_2 Adsorption on Amine-Grafted SBA-15: Elucidation of Adsorbed Species. *J. Phys. Chem. C* **2011**, *115* (23), 11540−11549.
(48) Tammer, M. G. Sokrates: Infrared and Raman Characteristic Group Frequencies: Tables and Charts. *Colloid Polym. Sci.* **2004**, *283* (2), 235.
(49) Marangon, V.; Hernández-Rentero, C.; Olivares-Marín, M.; Gómez-Serrano, V.; Caballero, A.; Morales, J.; Hassoun, J. A Stable High-Capacity Lithium-Ion Battery Using a Biomass-Derived Sulfur-Carbon Cathode and Lithiated Silicon Anode. *ChemSusChem* **2021**, *14* (16), 3333−3343.
(50) Alfonsetti, R.; Lozzi, L.; Passacantando, M.; Picozzi, P.; Santucci, S. XPS Studies on SiOx Thin Films. *Appl. Surf. Sci.* **1993**, *70*−*71*, 222−225.
(51) Finster, J.; Schulze, D.; Bechstedt, F.; Meisel, A. Interpretation of XPS Core Level Shifts and Structure of Thin Silicon Oxide Layers. *Surf. Sci.* **1985**, *152*−*153*, 1063−1070.
(52) Paparazzo, E.; Fanfoni, M.; Severini, E.; Priori, S. Evidence of Si-OH Species at the Surface of Aged Silica. *J. Vac. Sci. Technol., A* **1992**, *10* (4), 2892−2896.
(53) Hasa, I.; Passerini, S.; Hassoun, J. A Rechargeable Sodium-Ion Battery Using a Nanostructured Sb-C Anode and P2-Type Layered $Na_{0.6}Ni_{0.22}Fe_{0.11}Mn_{0.66}O_2$ Cathode. *RSC Adv.* **2015**, *5* (60), 48928.
(54) Lee, B.; Paek, E.; Mitlin, D.; Lee, S. W. Sodium Metal Anodes: Emerging Solutions to Dendrite Growth. *Chem. Rev.* **2019**, *119* (8), 5416−5460.
(55) Seh, Z. W.; Sun, J.; Sun, Y.; Cui, Y. A Highly Reversible Room-Temperature Sodium Metal Anode. *ACS Cent. Sci.* **2015**, *1* (8), 449−455.
(56) Ferrero, G. A.; Åvall, G.; Janßen, K.; Son, Y.; Kravets, Y.; Sun, Y.; Adelhelm, P. Solvent Co-Intercalation Reactions for Batteries and Beyond. *Chem. Rev.* **2025**, *125*, 3401−3439.
(57) Tian, Z.; Zou, Y.; Liu, G.; Wang, Y.; Yin, J.; Ming, J.; Alshareef, H. N. Electrolyte Solvation Structure Design for Sodium Ion Batteries. *Adv. Sci.* **2022**, *9* (22), 2201207.
(58) Liu, X.; Zhao, J.; Dong, H.; Zhang, L.; Zhang, H.; Gao, Y.; Zhou, X.; Zhang, L.; Li, L.; Liu, Y.; Chou, S.; Lai, W.; Zhang, C.; Chou, S. Sodium Difluoro(Oxalato)Borate Additive-Induced Robust SEI and CEI Layers Enable Dendrite-Free and Long-Cycling Sodium-Ion Batteries. *Adv. Funct. Mater.* **2024**, *34* (37), 2402310.
(59) Huang, Y.; Zhao, L.; Li, L.; Xie, M.; Wu, F.; Chen, R. Electrolytes and Electrolyte/Electrode Interfaces in Sodium-Ion Batteries: From Scientific Research to Practical Application. *Adv. Mater.* **2019**, *31* (21), 1808393.
(60) Hassoun, J.; Kimura, K.; Tominaga, Y. Cellulose-Based Electrolytes in Rechargeable Zn-Battery: An Overview. *Adv. Sustainable Syst.* **2025**, *9* (9), No. e00287.
(61) Bridel, J.-S.; Grugeon, S.; Laruelle, S.; Hassoun, J.; Reale, P.; Scrosati, B.; Tarascon, J.-M. Decomposition of Ethylene Carbonate on Electrodeposited Metal Thin Film Anode. *J. Power Sources* **2010**, *195* (7), 2036−2043.
(62) Marangon, V.; Barcaro, E.; De Boni, F.; Prato, M.; Bresser, D.; Hassoun, J. Effective Liquid Electrolytes for Enabling Room-Temperature Sodium-Sulfur Batteries. *Adv. Sustainable Syst.* **2024**, *8* (11), 2400268.
(63) Cheng, F.; Cao, M.; Li, Q.; Fang, C.; Han, J.; Huang, Y. Electrolyte Salts for Sodium-Ion Batteries: $NaPF_6$ or $NaClO_4$? *ACS Nano* **2023**, *17* (18), 18608−18615.
(64) Yan, Y.; Chen, G.; Liu, W.; Qu, M.; Xie, Z.; Wang, F. Pre-carbonization for Regulating Sucrose-Based Hard Carbon Pore Structure as High Plateau Capacity Sodium-Ion Battery Anode. *J. Energy Storage* **2024**, *104*, 114590.
(65) Mou, D.; Lin, Y.; Zhu, X. Sucrose-Anthracite Composite Supplemented by KOH&HCl Washing Strategy for High-Performance Carbon Anode Material of Sodium-Ion Batteries. *J. Power Sources* **2025**, *628*, 235924.
(66) Raspado, L.; Speyer, L.; Bolmont, M.; Cahen, S.; Fontana, S.; Hérold, C. Tuning the Porosity of Hard Carbons Elaborated from Sucrose. *J. Phys. Chem. Solids* **2024**, *191*, 112013.
(67) Zhao, Y.; Zhao, Y.; Zheng, J.; Lin, Y.; Liu, C.; Zheng, J.; Zhang, C.; Zhang, K.; Shen, Z. Designing Spherical Sucrose-Derived Hard Carbon Materials with Abundant Closed Pores via Amino-Aldehyde Condensation. *Energy Fuels* **2025**, *39* (12), 5974−5985.
(68) Carroll, A.; Grant, A.; Zhang, Y.; Gulzar, U.; Ahad, S. A.; Geaney, H.; O'Dwyer, C. Carbon Inverse Opal Macroporous Monolithic Structures as Electrodes for Na-Ion and K-Ion Batteries. *J. Electrochem. Soc.* **2024**, *171* (3), 030529.
(69) Nagmani; Puravankara, S. Insights into the Plateau Capacity Dependence on the Rate Performance and Cycling Stability of a Superior Hard Carbon Microsphere Anode for Sodium-Ion Batteries. *ACS Appl. Energy Mater.* **2020**, *3* (10), 10045−10052.
(70) Li, Y.; Xu, S.; Wu, X.; Yu, J.; Wang, Y.; Hu, Y.-S.; Li, H.; Chen, L.; Huang, X. Amorphous Monodispersed Hard Carbon Micro-Spherules Derived from Biomass as a High Performance Negative Electrode Material for Sodium-Ion Batteries. *J. Mater. Chem. A Mater.* **2015**, *3* (1), 71−77.
(71) Pan, Y.; Ji, B.; Wang, L.; Sun, Y.; Li, L.; Wu, X.; Zhou, P. Manipulating Micropore Structure of Hard Carbon as High-performance Anode for Sodium-Ion Batteries. *Electrochim. Acta* **2024**, *506*, 145042.

https://doi.org/10.1021/acs.energyfuels.5c06312
Energy Fuels 2026, 40, 3408−3422